# Simulation of Image-Guided Microwave Ablation Therapy Using a Digital Twin Computational Model

Frankangel Servin, Jarrod A. Collins, Jon S. Heiselman, Katherine C. Frederick-Dyer, Virginia B. Planz, Sunil K. Geevarghese, Daniel B. Brown, William R. Jarnagin, and Michael I. Miga

***Abstract*—Emerging computational tools such as healthcare digital twin modeling are enabling the creation of patient-specific surgical planning, including microwave ablation to treat primary and secondary liver cancers. Healthcare digital twins (DTs) are anatomically one-to-one biophysical models constructed from structural, functional, and biomarker-based imaging data to simulate patient-specific therapies and guide clinical decision-making. In microwave ablation (MWA), tissue-specific factors including tissue perfusion, hepatic steatosis, and fibrosis affect therapeutic extent, but current thermal dosing guidelines do not account for these parameters. This study establishes an MR imaging framework to construct three-dimensional biophysical digital twins to predict ablation delivery in livers with 5 levels of fat content in the presence of a tumor. Four microwave antenna placement strategies were considered, and simulated microwave ablations were then performed using 915 MHz and 2450 MHz antennae in *Tumor Naïve DTs* (control), and *Tumor Informed DTs* at five grades of steatosis. Across the range of fatty liver steatosis grades, fat content was found to significantly increase ablation volumes by approximately 29–l42% in the Tumor Naïve and 55–60% in the *Tumor Informed DTs* in 915 MHz and 2450 MHz antenna simulations. The presence of tumor did not significantly affect ablation volumes within the same steatosis grade in 915 MHz simulations, but did significantly increase ablation volumes within mild-, moderate-, and high-fat steatosis grades in 2450 MHz simulations. An analysis of signed distance to agreement for placement strategies suggests that accounting for patient-specific tumor tissue properties significantly impacts ablation forecasting for the preoperative evaluation of ablation zone coverage.**

***Index Terms*—Computational model, digital twin, fatty liver disease, finite element, liver cancer, microwave ablation.**

***Impact Statement*—This work provides a transformational framework for employing image-based biomarkers to create digital twins to enhance patient specificity, inform clinical decisions, and expand applications of microwave ablation to treat hepatic cancer.**

Manuscript received 1 June 2023; revised 14 August 2023, 25 October 2023, and 3 December 2023; accepted 4 December 2023. Date of publication 27 December 2023; date of current version 23 February 2024. This work was supported in part by Vanderbilt University under Grant NIH-R01EB027498 and Grant NIH-T32EB021937, and in part by Memorial Sloan Kettering Cancer Center under Grant P30CA008748. The review of this article was arranged by Editor Dieter Haemmerich. *(Corresponding author: Frankangel Servin.)*

Frankangel Servin is with the Department of Biomedical Engineering, Vanderbilt University, Nashville, TN 37235 USA, and also with the Vanderbilt Institute for Surgery and Engineering, Vanderbilt University, Nashville, TN 37235 USA (e-mail: frankangel.servin@vanderbilt.edu).

Jarrod A. Collins is with the Department of Biomedical Engineering, Vanderbilt University, Nashville, TN 37235 USA (e-mail: jarrod.collins@inarimedical.com).

Jon S. Heiselman is with the Department of Biomedical Engineering, Vanderbilt University, Nashville, TN 37235 USA, also with the Vanderbilt Institute for Surgery and Engineering, Vanderbilt University, Nashville, TN 37235 USA, and also with the Department of Surgery, Hepatopancreatobiliary Service, Memorial Sloan Kettering Cancer Center, New York, NY 10065 USA (e-mail: jon.s.heiselman@vanderbilt.edu).

Katherine C. Frederick-Dyer, Virginia B. Planz, and Daniel B. Brown are with the Department of Radiology, Vanderbilt University Medical Center, Nashville, TN 37235 USA (e-mail: kate.f-dyer@vumc.org; virginia.planz@vumc.org; daniel.b.brown@vanderbilt.edu).

Sunil K. Geevarghese is with the Department of Surgery, Vanderbilt University Medical Center, Nashville, TN 37235 USA (e-mail: s.geevarghese@vumc.or).

William R. Jarnagin is with the Department of Surgery, Hepatopancreatobiliary Service, Memorial Sloan Kettering Cancer Center, New York, NY 10065 USA (e-mail: jarnagiw@mskcc.org).

Michael I. Miga is with the Department of Biomedical Engineering, Vanderbilt University, Nashville, TN 37235 USA, also with the Vanderbilt Institute for Surgery and Engineering, Vanderbilt University, Nashville, TN 37235 USA, also with the Department of Radiology, Vanderbilt University Medical Center, Nashville, TN 37235 USA, also with the Department of Neurological Surgery, Vanderbilt University Medical Center, Nashville, TN 37235 USA, and also with the Department of Otolaryngology, Vanderbilt University Medical Center, Nashville, TN 37235 USA (e-mail: michael.i.miga@vanderbilt.edu).

Digital Object Identifier 10.1109/OJEMB.2023.3345733

## I. Introduction

BETWEEN 1980 and 2015, the incidence of primary liver cancer has more than tripled, with over 41000 people projected to be diagnosed in 2023 in the United States [1]. Similarly, in that same approximate period, mortality rates more than doubled, with over 29000 people dying in 2022. According to the American Cancer Society, approximately 70% of diagnoses are exacerbated by factors such as obesity, diabetes, and nonalcoholic fatty liver disease (NAFLD) [1]. In recent decades, these pathophysiologies have replaced alcohol-related factors

for developing hepatocellular carcinoma (HCC), which is the most common primary liver cancer [2], [3]. With respect to curative treatments for liver cancer, transplantation and resection are the primary considerations; however, the scarcity of livers and the eligibility for resection are both limited. As a result, locoregional therapies such as thermal ablation are commonly used as bridging therapies for resection or transplant. It is also important to note that thermal ablation plays a role in palliative cancer management and has been proposed as a first-line curative therapy in specific presentations of hepatic cancers [4], [5], [6].

While several ablation technologies exist, microwave ablation (MWA) is regarded as a favorable option for the locoregional treatment of liver cancer, particularly in patients with small ($\leq$2 cm in diameter) unresectable tumors [7]. Mechanistically, MWA is a thermal ablation interventional treatment where an antenna is navigated to the approximate center of a tumor, after which it is activated to induce dielectric hysteresis to desiccate tissue [8]. MWA is the contemporary counterpart to radiofrequency ablation (RFA) and has seen increasing adoption because of its faster delivery time, dose delivery characteristics, and improved patient outcomes [9], [10]. However, despite these favorable characteristics, typically 15–30% of patients receiving MWA therapy still suffer from tumor recurrence, especially those with tumors $\geq$ 3 cm [11]. These high rates of local tumor progression are primarily attributed to the incomplete coverage of the cancer's pathological extent by the necrotic ablation zone.

In response to these challenges, new antenna designs have been proposed to allow the ablation of larger tumors up to 4 cm in diameter, as well as the introduction of more precise directional targeting of tumors [12]. One design reported by [13] features an advanced directional targeting approach by employing a modified monopole radiating element and parabolic reflectors [14]. This design created directional heating patterns to sculpt targets in proximity to critical structures and avoid the need for piercing the tumor volume. Finite element simulations demonstrated that the proposed antenna had suitable impedance matching for insertion within a variety of tissue types. Additionally, ex vivo liver experiments revealed larger ablation zones in the forward direction when compared with prior designs [13], [14]. Another experimental approach is the use of thermal accelerants that are designed to augment microwave energy transmission, resulting in faster heating and larger ablation volumes [15], [16]. In a study by Maxwell et al., the use of thermal accelerants was associated with an average 40% increase in ablation volumes compared to standard ablations in in vivo swine (22.2 $cm^3$ vs 15.9 $cm^3$) as well as producing more spherical ablation volumes [17].

While these antenna-based and biological technologies can enable customized delivery, they do not address the question of how predictions can be tuned to a particular patient. Given the emergence of NAFLD as a serious etiological factor associated with liver cancer, incorporating patient-specific parameters associated with its progression could potentially enhance healthcare "digital twin" simulations beyond simple patient anatomy [18], [19]. Briefly described, NAFLD is the excessive influx of free fatty acids into hepatocytes which promotes triglyceride accumulation and creates a lipotoxic environment that causes hepatocyte cell death, liver inflammation, fibrosis, and pathological angiogenesis. This inflammatory response promotes fibrogenesis in the liver and drives disease progression [20]. Diagnostically, NAFLD severity is characterized by intrahepatic fat content, which can be measured using radiographic fat quantification imaging such as DIXON MR imaging. mDIXON imaging studies combine four or more DIXON sequences to create images that quantify fat, water, iron, and other chemical shift measurements [21]. These measurements can be combined to yield image volumes of estimated fat fraction, which are sampled to assess hepatic steatosis [22]. Pathologically, steatosis is graded from 0 to 3 based on triglyceride content, where grade 0 (low/normal) = $<$5%, grade 1 (mild) = 5%–33%, grade 2 (moderate) = 34%–66%, and grade 3 (severe) = $\geq$67% [23]. In mDIXON imaging, fat fraction ranges have been established in correspondence with histological grading, constituting grade 0 (low/normal) = $<$5%, grade 1 (mild) = 6%–17%, grade 2 (moderate) = 17%–22%, and grade 3 (severe) = $\geq$22% [24], [25]. Within the context of digital twin modeling, it is important to understand the impact of these underlying pathophysiological factors on MWA. More specifically, disease characteristics have been reported to influence the dielectric and thermal properties of biological tissue and, as a consequence, potentially affect thermal dose [26], [27], [28], [29]. These differences in thermal properties may be especially relevant for HCC because up to 30% of patients present concomitantly with fatty infiltration of the liver, and up to 70% experience liver fibrosis [11], [30], [31]. When considering the impact of fat on tissue-specific properties, the literature supports that thermal and dielectric properties differ between healthy liver and fat, with thermal conductivity, permittivity, and electrical conductivity being $\sim$2.5$\times$, $\sim$4$\times$, and $\sim$8$\times$ greater for healthy liver over fat, respectively [32]. Unfortunately, clinical dosing guidelines often estimate MWA lesion extent based on ex vivo experiments using healthy bovine or porcine livers [26], [33]. Similarly, little to no distinction is established in ablation forecasting models with respect to liver health and tumor tissue [26], [34], [35], [36]. This lack of alignment between device development experiments and the fundamental nature of disease processes such as fatty liver disease, inflammation, and fibrosis is concerning [37]. Furthermore, even if patients were stratified by steatosis grades, imaging studies have demonstrated that the spatial distribution of disease can be focal or diffuse with high levels of heterogeneity [37], [38], [39]. Ultimately, a clinical gap in understanding exists between clinical disease characteristics and current standards for appraising thermal ablation. However, advances in computational modeling and data science enable the creation of healthcare digital twins, which aim to construct comprehensive models driven by patient data to forecast therapeutic outcomes [19], [40], [41], [42]. The work presented herein is focused on addressing this gap by developing digital twin models to forecast patient-specific ablation margins under challenging liver cancer presentation.

In previous work, we proposed a computational framework to transform patient diagnostic and anatomical imaging data into a digital twin of thermal ablation with patient-specific but

homogeneous tissue parameters [43]. The imaging data were used in two roles: to segment the liver parenchyma, and to sample the liver fat and map material properties using characteristic equations derived from prior work in mock tissue phantoms. In this study, the work was extended in three ways. First, an enhanced digital twin was developed that maps *spatially heterogeneous* material properties based on each voxel of the fat fraction data. The grades of fat fraction were taken from a prior disease-state study. Second, ablation is simulated in a patient with an adenocarcinoma tumor which was sampled for fat content. Third, the patient vasculature was segmented to create realistic antenna positions for image-guided therapy delivery. The hypotheses being investigated are that tumor-property-informed digital twins will produce significantly different forecasts than traditional homogenous models, and that the choice of guidance trajectory of antenna placement is an important factor with respect to optimizing tumor destruction and the preservation of surrounding tissues. To test these hypotheses, to comprehensively integrate fat quantification data into a digital twin computational model, compare the forecasted ablation volumes against a model with homogenous material domains, and identify the importance of ablation placement strategies within digital twin simulations to inform therapeutic efficacy and treatment planning.

## II. Methods

This section details the creation and evaluation of a patient-specific digital twin MWA model incorporating heterogeneous tissue parameters from imaging data. First, a brief overview of the digital twin framework is provided. This section continues by describing the imaging data and image processing methods, the computational model associated with MWA, material description of liver tissue parameters, experimental conditions for investigation of image-guided MWA, and finally, the set of performance measures for ablation analysis.

### A. Analysis Overview

A digital twin framework presented in Fig. 1 is used in the study herein. It begins with acquiring patient-specific mDIXON magnetic resonance (MR) imaging data (Fig. 1(a)). The imaging data are used for three distinct roles: 1) The generation of a patient-specific three-dimensional computational finite element model of the organ anatomy (Fig. 1(b)). 2) The determination of spatially localized disease-related biomarkers, i.e., fat quantification, that are proposed as surrogates for patient-specific temperature-dependent dielectric and thermal properties (Fig. 1(c)). 3) To enhance preoperative planning, the hepatic and portal veins were segmented from contrast-enhanced images (Fig. 1(d)), and a custom algorithm was used to identify four placement strategies that navigated around the vasculature (Fig. 1(e)). Ablations were simulated in a 915 and 2450 MHz antennae, and both were powered at 60 W for 15 minutes, the maximum power and time for the MicroThermX Ablation System (Varian, Palo Alto, CA). Once completed, the ablation data were exported and processed to analyze ablation volume, tumor coverage, and damage to surrounding tissue (Fig. 1(e)).

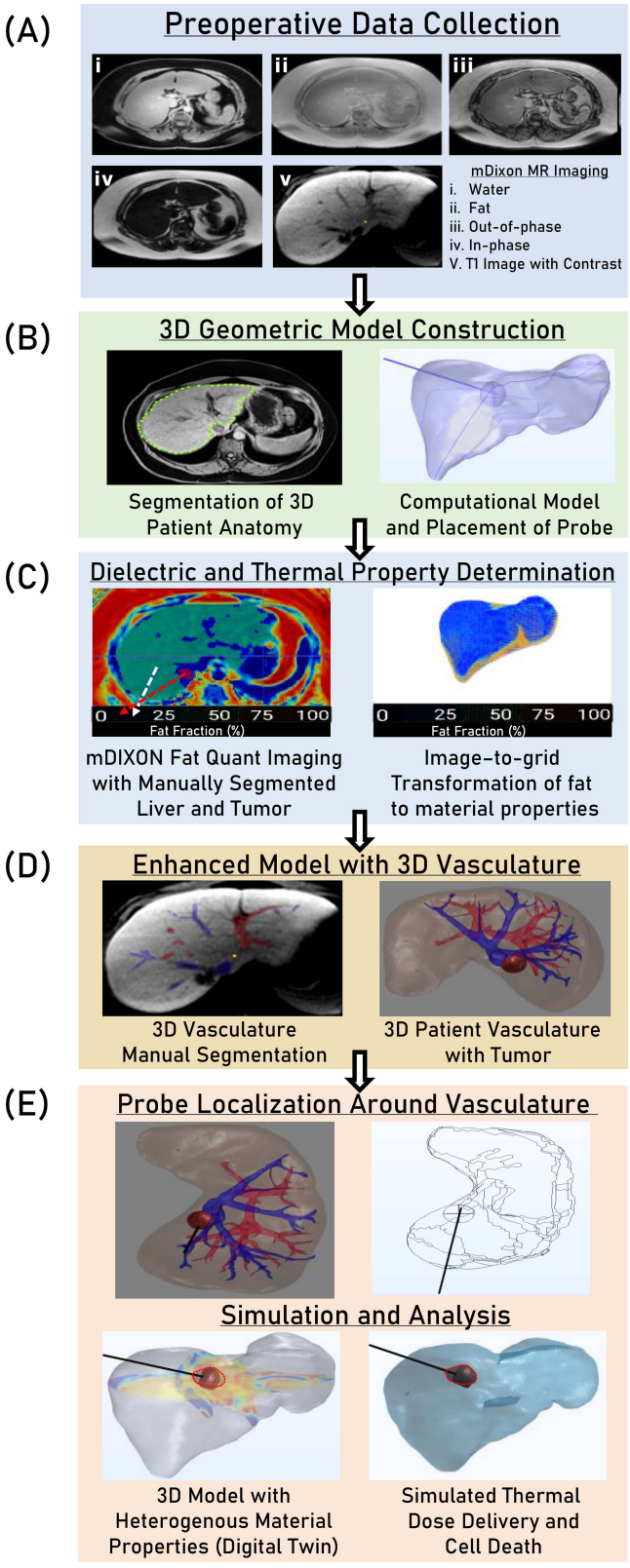


**Fig. 1.** Analysis overview with (a) mDIXON MR imaging, (b) patient-specific computational models with an implanted microwave antenna, (c) fat fraction image-to-grid heterogenous modeling strategy, (d) segmentation and mesh of hepatic and portal veins and the (e) antenna placement planning for image-guided surgery and the synthesis of a 3D MR-data-driven, patient-geometry-/heterogenous-material computational model (digital twin) with simulated microwave ablation.

To thoroughly investigate the local effects of tumor fat, two digital twins (DTs) are created, *Tumor Naïve* and *Tumor Informed*. *Tumor Naïve DTs* assume that the material properties of the tumor are the same as the surrounding parenchyma, while *Tumor Informed DTs* independently model tumor properties via patient-specific mDIXON fat fraction imaging. If the models demonstrate that tissue properties impact ablation margins, this would represent a consequential finding towards advancing the delivery of locoregional thermal ablation therapy delivery. In this work, the framework is employed using sampled fat fraction imaging data from four patients with varying liver fat infiltration (low, mild, moderate, and high), and one additional model was included to model a liver with no infiltrative fat. Overall, all 4 antennae placements simulated 5 fat contents, and combined with the 2 tumor models (Tumor Naïve and Tumor Informed) resulted in 40 simulations per antenna (915 MHz and 2450 MHz) to constitute 80 total simulations. The Memorial Sloan Kettering Cancer Center (MSKCC) and Vanderbilt University Medical Center (VUMC) Institutional Review Boards authorized the use of de-identified imaging data obtained from one patient in a bystander study at MSKCC and three patients for retrospective analysis at VUMC for this research.

### B. Imaging and Image Processing

MR imaging data from four patients were retrieved by experienced physicians at MSKCC and VU with the goal of ensuring that appropriate patients were considered that received high-quality fat quantification and contrast-enhanced anatomical scans. MR imaging data was obtained from a Philips Intera Achieva 3T MR clinical scanner at VUMC and a GE SIGNA Artist 1.5T MR clinical scanner at MSKCC. Clinically available mDIXON sequences (2.38 ms TE, 1.1 ms TR and 4.6 ms TE, 2.3 TR ,respectively) were acquired to generate in-phase, out-of-phase, water, and fat image volumes with voxel resolutions ranging from 1.953 mm × 1.953 mm × 3.0 mm to 2.083 mm × 2.083 mm × 5.0 mm over a transverse field of view [44], [45], [46]. In addition, contrast-enhanced T1 image volumes were acquired at a resolution of .9766 × .9766 × 2.5 mm and co-registered to the mDIXON image volume. Images in Fig. 1(a) depict MR images of the water content, fat fraction, out-of-phase, in-phase, and a T1 image with contrast for one patient.

The percentage thresholds to stratify fat infiltration levels were based on clinically defined thresholds [24], [25]. Fig. 2(a)–(d) depict segmented fat fraction images for a low-, mild-, moderate-, and high-fat patient, and Fig. 2(e) displays a normalized histogram of the fat content for each. It is noteworthy to observe the considerable variance in fat percentages within an individual liver for each patient and among the patient cohort. In previous work, it was demonstrated that in the case of distributed (non-focal) fat deposition, a voxel-by-voxel mapping of changes due to disease performed very similarly to a model that assumed homogeneity but at the corresponding diseased state grade [47]. While it may be sufficient to model the parenchyma using homogenous material properties under some conditions, fat quantification values associated with the tumor, however, demonstrated to be a significant heterogeneity as compared to the surrounding parenchyma.

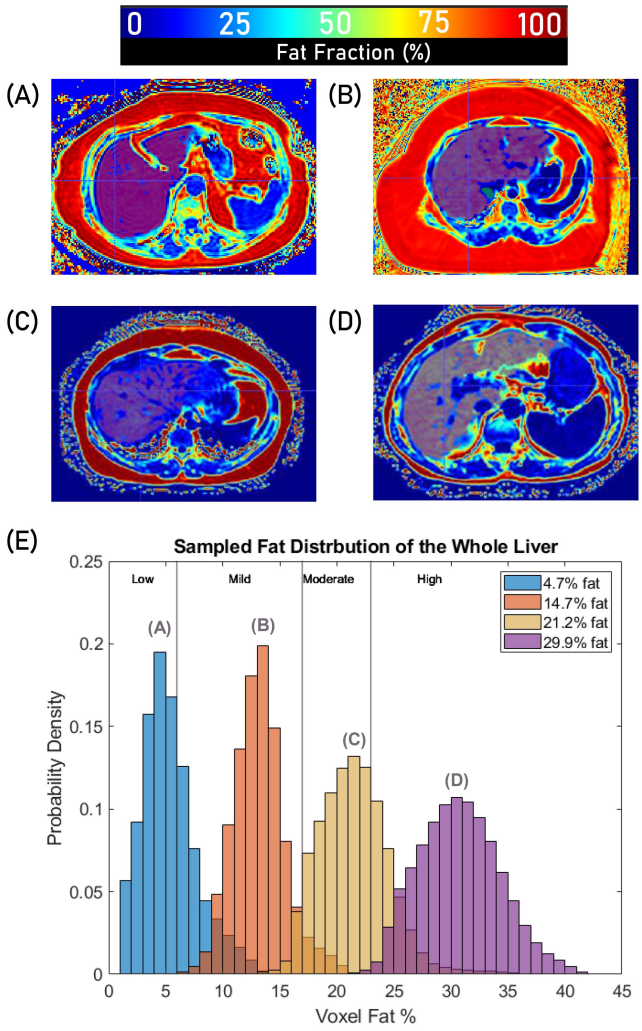


**Fig. 2.** (a)–(d) Fat fraction image with liver fat segmented (shown as a semi-transparent red overlay) in patients with low-fat (a), mild-fat (b), moderate-fat (c), and high-fat (d). (e) Histogram of fat-encoded intensity values of 4 patients belonging to different steatosis grades (low, mild, moderate, high). The average fat percentages are shown in legend.

### C. Computational Model

With respect to the biophysical computational model, the 3D finite element model was created in COMSOL Multiphysics 5.6 (COMSOL Inc, Burlington, MA) to simulate electromagnetic wave propagation and heat transfer in a patient-specific liver model in 915 and 2450 MHz coaxial antennas with a single ring slot powered at 60 W for 15 minutes [48]. The mesh resolution was set as 0.02–2 mm for the tumor and microwave antenna and 0.5–3 mm for the liver. For every time step, the convergence criterion error tolerance was set to $1e^{-6}$. The propagation and absorption of electromagnetic waves radiating from the antenna in the model, assuming no existing charge, is described by a simplified form of Maxwell's electromagnetic wave equation in

three dimensions in the frequency domain,

$$\nabla \times \left( \mu_r^{-1} \nabla \times \vec{E} \right) - \frac{\omega^2}{c_0^2} \left( \varepsilon_r - \frac{j\sigma}{\omega \varepsilon_0} \right) \vec{E} = 0 \quad (1)$$

where the material properties are the relative permeability $\mu_r^{-1}$, relative permittivity $\varepsilon_r$, and electrical conductivity $\sigma$ [S/m]. $\omega$ [rad/s] is the angular frequency of the electromagnetic wave, $c_0$ [m/s] is the speed of light in a vacuum, and $\vec{E}$ [V/m] is the electric field strength. Boundary conditions followed the work of [49] and invoked an applied scattering condition at the exterior of the liver to enable the effect of transparent transmission, core conductive material realized as $\vec{n} \times \vec{E} = 0$, and the source modeled as a port boundary condition. The microwave source was modeled as a port boundary condition adopted from COMSOL (1998–2023b) and was simulated via the S-parameter port boundary conditions,

$$S = \frac{\int_{port\ 1} \left( \left( E_c - E_1 \right) E_1^* \right) dA_1}{\int_{port\ 1} \left( \left( E_c * E_1 \right) E_1^* \right) dA_1} \quad (2)$$

where $E_c$ is excitation plus the reflected field, $E_1$ is the electric field of the port, and $A_1$ is the area of the port boundary [50]. Electromagnetic waves were modeled as perfectly matched layers. Heat transfer was modeled using Pennes' Bioheat equation,

$$\rho C_p \frac{\partial T}{\partial t} = \nabla \cdot k \nabla T + \left( \rho_b C_{p,b} \omega_b \right) \left( T - T_b \right) + \frac{1}{2} \sigma \left| \vec{E} \right|^2 \quad (3)$$

where $\rho$ [kg/m$^3$] is mass density, $C_p$ [3450 J/kg·K] is the isobaric heat capacity of liver tissue, $k$ [W/m·K] is thermal conductivity, $T$ [K] is the current temperature, $\rho_b$, $C_{p,b}, \omega_b$, and $T_b$ are the density [1000 kg/m$^3$], isobaric heat capacity [J/kg·K], perfusion rate [1/s], and temperature [37 °C/ 310 K] of blood, respectively [51]. The first term $\nabla \cdot k \nabla T$ is a conservation statement regarding heat flux using Fourier's Law for heat conduction. The second term $(\rho_b C_{p,b} \omega_b)(T - T_b)$ describes heat loss by blood perfusion. The third term $\frac{1}{2}\sigma |\vec{E}|^2$ is heat generation due to absorbed electromagnetic energy in [W/m$^3$]. Boundaries along the liver parenchyma were set to the temperature of the human body (37 °C). Internal boundaries between the phantom and ablation antenna simulated saline cooling within the antenna with a convective heat flux condition,

$$\vec{n} \cdot (-k \nabla T) = h \cdot (T - T_{ext}) \quad (4)$$

where $\vec{n}$ is the normal vector to the element, $k$ [W/m·K] is the thermal conductivity, $h$ [980 W/m$^2$·K] is the heat transfer coefficient, $T$ [K] and $T_{ext}$ are the current temperature, and the saline temperature [23 °C/300 K], respectively [48], [51]. Taken in their entirety, (1) and (3) account for heat transfer, heat storage, and perfusion exchange in a living tissue modeled as a solid medium exposed to a microwave electromagnetic field. While (3) provides a distribution of thermal energy over time, it does not express the level of thermal damage, which is associated with a temporally evolving thermal dose.

More specifically, thermal tissue injury is conventionally expressed with the Arrhenius damage integral. In (COMSOL, 1998–2022a), the degree of thermal injury, $\alpha$, is defined by the temporally evolving Arrhenius integral,

$$\alpha(t) = \alpha_0 + \int_0^{t'} \left( A e^{-\Delta E / RT(t)} \right) dt \quad (5)$$

The degree of tissue injury over time, $\alpha(t)$, is a function of initial injury $\alpha_0$, frequency factor $A$ [7.39$*$10$^{39}$ 1/s], activation energy $\Delta E$ [2.577$*$10$^5$ J/mol] to induce tissue damage, the universal gas constant $R$ [8.314 J/mol·K], and temperature history of the liver tissue $T(t)$ [K]. The fraction of damaged tissue ($\theta_d$) can then be determined by,

$$\theta_d = 1 - e^{-\alpha(t)} \quad (6)$$

where $\theta_d$ represents the percentage of cell death. A threshold of $\theta_d > 0.98$ was used to indicate cell necrosis. This specific Arrhenius expression produces values in range of 0-1, where 1 indicates complete cellular destruction, and has been established to accurately calculate necrosis resulting from thermal damages [52], [53], [54], [55], [56]. While the above discusses the biophysical phenomenon of microwave ablation, the relationships that will establish the specificity of the digital twin regarding how disease factors affect simulation predictions need to be defined.

### D. Constitutive Equations for Material Properties

***1) Mapping Properties Based on Fat Fraction Biomarkers:*** Fat fraction values were used in the context of mapping functions for biophysical properties. In mDIXON imaging, the fat-to-water signal ratio establishes a fat fraction parameter, which represents the percentage of fat in a given volume of tissue [22]. The intensities of the fat fraction image were directly mapped into material properties and imported into the digital twin finite element model [47]. A material mixture equation to describe fat-dependent dielectric and thermal material properties is expressed as follows,

$$m(f\%) = \left( \left( m_{liver} - m_{fat} \right) e^{-\tau_k * f\%} \right) + m_{fat} \quad (7)$$

Where $f\%$, $m_{liver}$, $m_{fat}$ are the fat fraction percentage derived from imaging data, the material property value ($m$) sought for liver and fat, respectively (note, the fitting (7) was used for all properties). The exponential factor $e^{-\tau_k}$ was derived from a previous mock tissue phantom study and is listed in Table I [48]. It is important to note that parenchymal liver and tumor are treated somewhat differently in the deployed use of (7). Table I lists the dielectric, thermal, and perfusion properties of liver parenchymal tissue at all steatosis grades as one specific value, i.e., a homogeneous value within the liver parenchyma. For this determination, the average fat percentage (determined by mDIXON image analysis) across the entire liver (excluding vasculature) was calculated and then used within the context of (7) to estimate the respective liver parenchymal material property. This approach reflects previous work in which it was found that the difference in therapy simulations was minima when comparing a homogeneous description versus a mapping of properties voxel-by-voxel within the context of diffuse disease [47]. Given that the patients in this study presented with diffuse fatty liver disease, this approach was appropriate for the liver parenchyma. However, while the presence of intertumoral fat

**TABLE I**
MATERIAL PROPERTIES

| **Patient Fat Infiltrative Index** | 0 | 1 | 2 | 3 | 4 | * | * | * |
|---|---|---|---|---|---|---|---|---|
| Steatosis Grade | No-Fat (*Liver*) | Low (0-6%) | Mild (6-17%) | Moderate (17-22%) | High (>22%) | *Tumor* | *Fat* | $-\tau_k$ |
| Average Fat Percent (%) | 0 | 4.66 ± 2.80 | 12.67±2.25 | 21.20±2.90 | 29.90±3.7 | 5.56±2.90 | 100% | * |
| Thermal Conductivity [W/(m·K)] (915 MHz) | 0.521 | 0.451 | 0.364 | 0.309 | 0.270 | 0.44±0.03 | 0.21 | .012 |
| Electrical Conductivity [S/m] (915 MHz) | 0.861 | 0.821 | 0.757 | 0.699 | 0.641 | 0.81±0.23 | 0.11 | .069 |
| Electrical Conductivity [S/m] (2450 MHz) | 1.69 | 1.62 | 1.496 | 1.384 | 1.273 | 1.60±0.23 | 0.268 | .069 |
| Permittivity [1] (915 MHz) | 46.8 | 44.9 | 42.0 | 39.3 | 36.5 | 44.6±1.1 | 10.8 | .067 |
| Permittivity [1] (2450 MHz) | 43.0 | 41.0 | 37.9 | 35.0 | 32.1 | 40.7±1.1 | 5.28 | .067 |
| Perfusion Mass Flow Rate [$\rho\omega$] (kg/m$^3$*s) | 18 | 17 | 15 | 14 | 13 | — | — | * |

Steatosis grade index and the corresponding average percent fat derived from the fat quantification imaging data for each patient. Material properties at a particular steatosis grade were determined using the material characteristic curves established in previous work but with a modified scale based on the human data range [43], [49]. For liver parenchyma, an average fat percentage value across the entirety of the liver was used within Equation (7) to produce a homogenous tissue property. In the case of *Tumor Informed Digital Twin*, a voxel-by-voxel fat fraction value within the tumor imaging data using Equation (7) was employed for a highly heterogeneous property description. With each tissue type, properties are provided, as well as the exponential factor $\tau_k$ associated with Equation (7) model.

in hepatic cancer is widely acknowledged, the dielectric and thermal material properties of fatty tumors are not as well understood [57], [58]. Given that the tumor tissue is in close proximity to the microwave excitation source, the digital twin models favored a voxel-by-voxel mapping of material properties using (7) throughout the segmented tumor volume. Finally, blood perfusion $\omega_b$ is described to vary between healthy and cirrhotic liver perfusion values as a function of fat fraction percentage as well with complete cirrhotic perfusion rates saturating at a fat fraction of 35% [24], [25], [59].

***2) Incorporating Thermally Dependent Material Performance:*** Modeled liver and tumor tissue, as described in (7), allows the computational model to modify its material properties in response to fat content within the tissue. However, this description is insufficient, as MWA involves rapid tissue desiccation through water vaporization [60]. To accurately replicate this process, the model must also account for thermal changes and water loss that occur within the liver tissue by incorporating temperature-dependent material properties. The approach adopted in this work follows the experimental work of Silva et al., who validated their mathematical expressions against reported ex vivo data investigating thermal properties [29]. The analytical function describes the characteristics change of each material property – i.e., thermal conductivity and volumetric heat capacity – as a function of temperature (T) in the range from 20 °C to 100 °C,

$$Y(T) = a + b{*}e^{cT} \tag{8}$$

with $a$, $b$, and $c$ as regression coefficients that fit the data values from the experiments and associated literature. The coefficient $a$ is associated with the initial value of the material property. For thermal conductivity, because the digital twin represents heterogeneous material properties, $a$ is defined as the material property at each voxel according to (7). When graphing (8), thermal conductivity remains at a relatively constant value until liver tissue reaches approximately 70 °C, which then experiences a 2-fold increase in value. Similar behaviors have been reported in ex vivo tissue experiments and were directly referenced by Silva et al. [28], [61], [62]. Due to the lack of extensive data on the effects of infiltrative liver fat on volumetric heat capacity, the digital twin simulations consider this property to remain constant. Additionally, the equation establishes that volumetric heat capacity is relatively constant until liver tissue reaches approximately 65 °C and experiences a greater than two-fold increase and peaks at 100 °C. For this work, the coefficients for $a$, $b$, and $c$ for each thermal property were derived from the regression work by Silva et al. are reported in Table II (note, the value of $R^2$ from that fitted work ranged from 0.93–0.95) [29]. Tissue that exceeds 100 °C was assigned to have properties as described by Deshazer et al., where thermal conductivity is modeled as [26]

$$k\,(T > 100\,^{\circ}\mathrm{C}) = k * (1 - .00092 * (100\,^{\circ}\mathrm{C} - 37\,^{\circ}\mathrm{C})) \tag{9}$$

Volumetric heat capacity above 100 °C returned to baseline values, as there is insufficient data to predict values above 100 °C [29], [62].

**TABLE II**
TISSUE THERMAL REGRESSION MODEL

| **Thermal Property** | *a* | *b* | *c* |
|---|---|---|---|
| Thermal Conductivity $k$ [W/(m·K)] | $K\,(f\,(\%))$ eq. (7) | 1.447*10$^{-11}$ | .256 |
| Volumetric Heat Capacity $C_p$ [MJ/(m$^3$·K)] | 3.415 | 1.278*10$^{-12}$ | .289 |

Regression coefficients associated with Equation (8) and based on the modeling fitting from Silva et al. [29].

## *E. Dielectric Properties of Tissue*

Dielectric properties of liver tissue are dependent on the excitation radiofrequency. In this work, two clinically relevant excitation frequencies were used in our mock antennae, 915

MHz and 2450 MHz [63]. Electrical conductivity ranged from 0.79–0.88 [S/m] at 915 MHz and 1.68–1.95 [S/m] at 2450 MHz. For 915 MHz, an electrical conductivity of 0.861 [S/m] was selected as the baseline for tissue with no infiltrative fat [37], [64]. For 2450 MHz, O'Rourke et al. measured the electrical conductivity and relative permittivity of an ex vivo tissue sample and reported that healthy tissue had an electrical conductivity of 1.68 [S/m] [65]. For this study, at 915 MHz and 2450 MHz, the electrical conductivity of fat was approximately 0.268 [S/m] from Hasgall et al. [37]. With respect to relative permittivity, liver tissue is greater than fat, with estimates of 45.8 to 50.8 for liver tissue and 10.8 for fat at 915 MHz [32], [66]. In this study, the relative permittivity for liver tissue without infiltrative fat was considered to be 46.8 for 915 MHz and 43.0 at 2450 MHz.

For both frequencies, it can be inferred that the electrical conductivity and permittivity decreases when the liver has increased intra-tumoral fat. However, with respect to current knowledge, the relationship between fat infiltration and dielectric properties are unknown. A previous investigation by Collins et al. fit a mathematical relationship between electrical conductivity and fat in a mock liver tissue phantom that consisted of agar, albumin, and varying percentages of fat content [48]**.** Similar to previous experiments [43], initial values from Hasgall et al. and Curto et al. were used to seed the mixture model of (7). The parameter values are reported in Table I. Recall, fat quantification imaging data for all subjects reflected a diffuse disease presentations fatty liver disease. As a result, dielectric properties of the liver were assumed homogenous within digital twin simulations of each patient and were modeled using the average material property values as reflected in Table I.

Concerning the effect of local tumor tissue properties on MWA, previous studies estimated that hepatic tumors had conductivity values between 0.88–1.99 [S/m] and relative permittivity values between 57.09–54.88 at frequencies between 915 MHz and 2450 MHz [65]. Specifically, O'Rourke et al. estimated that the conductivity of tumor tissue is approximately 26% greater than the surrounding tissue, while relative permittivity is approximately 20% greater [65]. In this study, tumor tissue was assigned its electrical conductivity and relative permittivity according to material relationships associated with fat quantification imaging, (7), and voxel-by-voxel. It is interesting to note that when sampling the original imaging scan, there was a 50% difference in liver fat between the tumor and the surrounding liver parenchyma (6% vs. 14%, respectively). Although the metastatic colorectal carcinoma (mCRC) in this study did not exhibit the identical percentage increase as indicated by O'Rourke et al., it is noteworthy that the fat quantification parameterization yielded higher conductivity and relative permittivity compared to the surrounding parenchyma (a common assumption in models that involve dielectric properties) [65]. This discovery implies the potential use of imaging biomarkers, such as fat quantification imaging, as proxies for tissue properties. For the *Tumor Naïve DTs*, the tumor is assumed to have the same fat content as the surrounding parenchyma. For the *Tumor Informed DTs*, the voxel spatial heterogeneity from the *acquired imaging data* was translated into material properties directly.

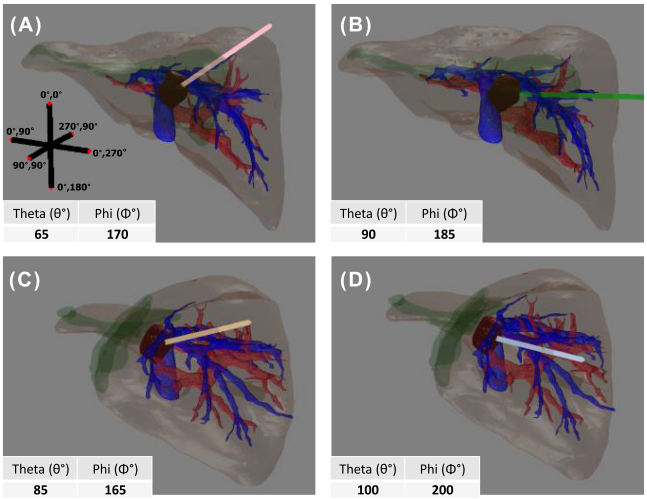


**Fig. 3.** Liver (brown) with 4 hypothetical antenna placements (a)–(d) (pink, green, tan, and blue, respectively) targeting the center of the mCRC tumor (brown). Additionally, the major vasculature of the hepatic vein (blue) and portal vein (red) are depicted. The bare area of the liver is highlighted (green) and the reference system is shown in A ( $\theta^{\circ}, \Phi^{\circ}$).

### F. Thermal Properties of Tissue

Reported values for thermal conductivity ($k$) in healthy livers range from 0.48–0.54 [W/m·K] independent of antenna frequency. Early literature sources report thermal conductivity at approximately 0.48 [W/m·K], but these estimations were derived from tissue experiments at room temperature (25 °C) [67]. A more recent study from Mohammadi et al. describes the thermal conductivity of ex vivo porcine liver submerged in a heated water bath as a function of temperature where the thermal conductivity was as high as $0.537 \pm 0.009$ [W/m·K] at body temperature (37 °C) [62]. Another study by Guntur et al. calculated the thermal conductivity of ex vivo porcine liver at 37 °C to be approximately 0.520 [W/m·K ] [27]. For this work, an estimate of 0.52 [W/m·K ] was selected as the baseline thermal conductivity for tissue with no infiltrative fat, following the values given by [32] and supported by Guntur et al. For the variations in thermal conductivity as a function of fat content, (7) was employed; and as noted, an average value for the liver parenchyma, and a voxel-by-voxel mapping within the tumor based on fat percentage values were used.

### G. Antenna Targeting Strategy

In addition to the liver parenchyma and tumor structures, the anatomic features of the hepatic and portal vasculature were segmented using 3D Slicer [56]. All structures were imported into MATLAB (Mathworks, Natick, MA) and then used within a custom planning utility to create four candidate placement strategies (Fig. 3). For reference, image-guided MWA interventions typically involve patients placed in the supine position and rotated to facilitate access to the left or right side of the liver [8], [57]. In the patient presented in Fig. 3, the tumor was located in segment 7 with approximate Feret dimensions of $24 \times 35 \times 28$ mm$^3$ and volume of 11.7 cm$^3$ [68]. Its near-organ-surface

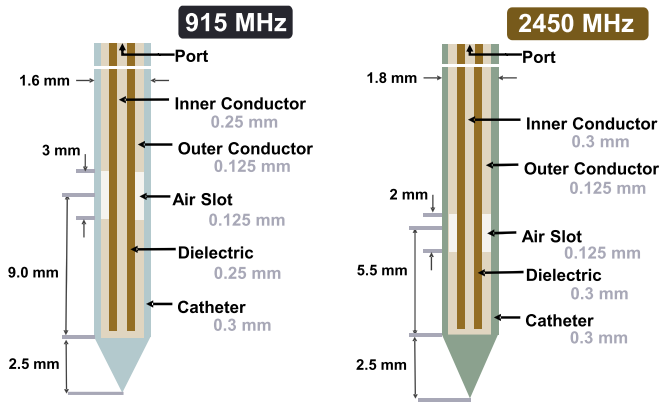


**Fig. 4.** Diagram of the 915 MHz antenna modeled after a single-slot SynchroWave ST Probe (Varian, Palo Alto, CA) [48]. and a single-slot 2450 MHz antenna modeled from Cocic et al. [34].

position posterior to the right hepatic vein and proximal to the diaphragm allows the right side to be more accessible to interventional MWA trajectories for delivery. To maintain clinical guidelines, antenna placement strategies fulfilled the following criteria: All antenna trajectories were ≥5 mm away from the vasculature and angled as close to the coronal plane as possible (for accessibility), and the antenna slot targeted the center of the tumor [57]. Fig. 3 illustrates the orientation of the candidate antennas, with the theta ($\theta$) and phi ($\Phi$) angles described in relation to the center of the tumor. Placement A is posterior to the right hepatic vein and approaches from above the branch. Placements B, C, and D are anterior to the right hepatic vein; B is angled along the transverse plane, and C and D are positioned between the secondary branches of the right hepatic vein. With respect to the ribcage, the trajectories of placements C and D faced away from the ribcage, but placements A and B partially intersected with the ribcage and may require hydrodisection to access [69]. The 915 MHz antenna was modeled after a SynchroWave ST Probe (Varian, Palo Alto, CA) employed in prior research, and the 2450 MHz antenna was designed by modifying this design according to other 2450 MHz antenna designs described in the literature [29], [39], [44], [58]. For reference, the schematics of the two antennae are depicted in Fig. 4 Lastly, it should be noted that current clinical guidelines would not consider this patient for MWA, given the size and location of the tumor. However, its selection for this study enables comparisons among approaches within the context of MWA for speculative advances in therapeutic capabilities for this treatment modality. Considering current constraints on ablation zone size and shape characteristics, it is anticipated that the whole lesion cannot be completely ablated with a single conventional 915 and 2450 MHz antenna in this work; but the results will allow us to understand the spatial differences in ablation under variable disease in a controlled manner.

### H. Ablation Analysis

The ablation volume was calculated in MATLAB (Mathworks, Natick, MA) using exported data from COMSOL. More specifically, COMSOL computes the Arrhenius integral value, (5), throughout the finite element mesh over a temporally evolving thermal distribution. The experimental procedure involved a 15-minute ablation simulation, during which solutions were collected at 15-second intervals. A value of $\theta_d \geq 0.98$ for the integral was used as a threshold to determine the necrotic tissue volume. Element volumes that met the threshold ablation were then summed to produce the total ablated volume. To approximate Feret diameter measurements [68], [70], [71], the short-axis and long-axis were calculated by fitting an ellipsoidal surface to the ablation volume. Ablation volumes were analyzed in the following manner: 1) The final ablation volume and axis dimensions within the same disease presentation were compared using a series of paired *t*-tests at a significance level of 0.05 across all placement strategies to determine the effects of tumor heterogeneity. 2) The final ablation volume and axis dimensions were calculated and tabulated to allow for comparison among antenna types. 3) The signed distance to agreement (SDA) was used to assess the optimization of placements for tumor coverage and surrounding tissue preservation, particularly due to the close location of the tumor to the inferior vena cava and right hepatic vein. The SDA was calculated using the distance, $d(A,\ \Omega)$, between the ablation boundary point coordinates $(A)$ from the finite element simulation and the nearest exterior point coordinates $(\Omega)$ of the tumor boundary mesh segmented from the original imaging data. The geometric expression is,

$$d\left(A,\ \Omega\right) = \sqrt{\left(\Omega_{\mathrm{x}} - A_x\right)^2 + \left(\Omega_{\mathrm{y}} - A_y\right)^2 + \left(\Omega_{\mathrm{z}} - A_z\right)^2} \tag{10}$$

where each *(x, y, z)* point coordinate of $(A)$ is utilized. Following the protocol for measuring isothermal dosing, each point was identified as either being within the tumor or outside the tumor boundary, resulting in a negative and positive signed distance to agreement, respectively [72]. Assuming and $A_i$ as a single point on the ablation boundary and $\Omega$ as the tumor volume, the signed distance to agreement between ablation and tumor is defined as,

$$SDA_{A-T}(x) = \begin{cases} -d\left(A_i,\ \delta\Omega\right) & \text{if } A_i \in \Omega \\ d\left(A_i,\ \delta\Omega\right) & \text{if } A_i \notin \Omega \end{cases} \tag{11}$$

In summary, $\mathrm{SDA_{A\text{-}T}}$ color encodes the ablation volume produced whereby negative values indicate successfully ablated tumor while positive values represent extra-tumoral ablation. $\mathrm{SDA_{T\text{-}A}}$ is the contra-indicative calculation, and color encodes the tumor volume whereby negative values indicate ablated tumor while positive values represent regions likely to recur as they did not successfully reach the Arrhenius threshold. Fig. 5 presents a schematic of $\mathrm{SDA_{A\text{-}T}}$ and $\mathrm{SDA_{T\text{-}A}}$ metrics.

## III. Results

Table III reports the average final ablation volume, long-axis diameter, and short-axis diameter across *Tumor Naïve* and *Tumor Informed DTs* for the 915 MHz antenna. When comparing the size of necrotic volumes with and without a tumor in the presence of equivalent NAFLD disease states, there was no

**TABLE III**
ABLATION ZONE MEASUREMENTS 915 MHz

| **Patient Fat Content Index** | 0 | 1 | 2 | 3 | 4 |
|---|---|---|---|---|---|
| Steatosis Grade | No Fat (0-6%) | Low (0-6%) | Mild (6-17%) | Moderate ( 17-22%) | High (>22%) |
| **Results in *Tumor Naïve* Digital Twin** | | | | | |
| Long-Axis Diameter (cm) | 5.67±0.10 | 6.00±0.16 | 6.04±0.67 | 6.64±0.80 | 6.95±0.72 |
| Short-Axis Diameter (cm) | 1.75±0.10 | 1.77±0.09 | 1.82±0.10 | 1.83±0.16 | 1.84±0.13 |
| Ablation Volume ($cm^3$) | 8.81±0.25 | 9.57±0.54* | 9.96±0.59 | 10.82±0.69 | 12.58±0.52* |
| **Results in *Tumor Informed* Digital Twin** | | | | | |
| Long Axis-Diameter (cm) | 5.78±0.02 | 5.98±0.11 | 6.26±0.19 | 6.84±0.23 | 7.06±0.19 |
| Short Axis-Diameter (cm) | 1.69±0.11 | 1.76±0.11 | 1.86±0.10 | 1.93±0.18 | 2.12±0.14 |
| Ablation Volume ($cm^3$) | 8.26±0.19 | 9.19±0.36** | 10.47±0.36** | 11.39±0.86 | 13.23±0.51* |

**P<.05 **P<.01

† = P<.01

**reports a greater metric when compared to the corresponding metric of the preceding, lower fat content**

**reports a greater metric when compared to the corresponding metric within the same fat content between digital twins**

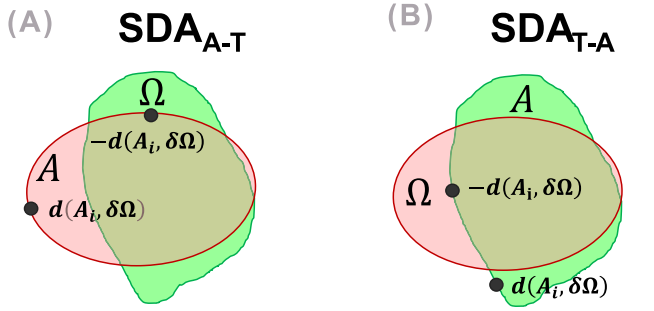


**Fig. 5.** Schematic of signed distance to agreement between ablation zone (red) and tumor (green): (a) $SDA_{A-T}$ color-codes the ablation volume where negative values indicate ablated tumor and positive values indicate extra-tumoral ablation (b) $SDA_{T-A}$ color-codes the tumor volume where negative values indicate ablated tumor and positive values are recurrence regions.

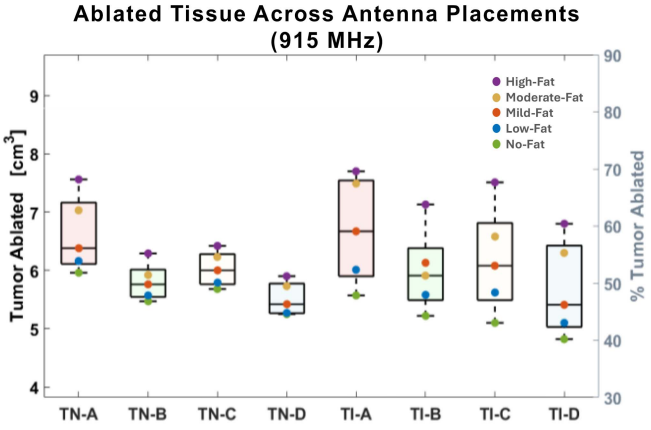


**Fig. 6.** Boxplot of the final tumor ablated volume ($cm^3$) and percent (%) tumor ablated (915 MHz antenna, 15 minutes at 60 W power) across all fat contents and antenna placements (A-D) in *Tumor Naïve (TN)* and *Tumor Informed (TI)* digital twins. Original tumor volume is 11.7 $cm^3$.

significant difference in all instances. Examining the effects of fatty liver disease within each group, no-fat vs. low-fat and moderate-fat vs. high-fat livers had significantly increased ablation volumes for these comparisons. Only the *Tumor Informed DTs* were significantly different when comparing low-fat vs. mild-fat ablation volumes. It should be noted that when interpreting Table III, significance with respect to disease state was only tested with respect to neighboring states.

Fig. 6 Presents the results in the context of varying the fat content in the four antenna placements and the presence of tumors explicitly modeled for the 915 MHz ablations. When ranking each placement based on the ablated tissue across all fat contents, Placement *A* resulted in the most tumor damage, followed by *C*, *B*, and *D*. Comparing the ablation of surrounding tissue vs. tumor tissue, approximately 5.25–7.10 $cm^3$ and 4.80–7.70 $cm^3$ (50–68% and 45–70%) of ablated tissue was tumor tissue in *Tumor Naïve*, and *Tumor Informed* DTs, respectively. Intriguingly, the tumor damage in no-fat and low-fat content was greater in the *Tumor Naïve DTs*, while the *Tumor Informed DTs* had greater volumes in mild-, moderate-, and high-fat livers.

Fig. 7 depicts the signed distance to agreement ($SDA_{A-T}$) between the boundary points of the final ablation volume (time = 15 minutes) and tumor volume accompanied by the ($SDA_{T-A}$) between the edges of the tumor and the boundary points (BPs) in high-fat livers with the 915 MHz antenna. The $SDA_{A-T}$ from *Tumor Naive* and *Tumor Informed* DTs demonstrate similar distributions within corresponding placement strategies, indicating a similar proportion of tumor coverage. The $SDA_{T-A}$ communicates that all placements resulted in a central ablation surrounded by a tumor remnant. *A* and *C* were the closest in ablating the superior portion of the tumor, yet also resulted in the least coverage in the inferior portion of the tumor. *B* and *D* overall had modest coverage in all portions of the tumor but ultimately resulted in the least ablated tumor volume.

Table IV reports the average final ablation volume, long-axis diameter, and short-axis diameter across *Tumor Naïve* and *Tumor Informed DTs* using the 2450 MHz antenna. Analysis of the necrotic volumes indicates that tumor characteristics (i.e.,

**TABLE IV**
ABLATION ZONE MEASUREMENTS 2450 MHZ

| **Patient Fat Content Index** / Steatosis Grade | 0 No Fat (0-6%) | **1** Low (0-6%) | **2** Mild (6-17%) | **3** Moderate ( 17-22%) | **4** High (>22%) |
|---|---|---|---|---|---|
| **Results in *Tumor Naïve* Digital Twin** | | | | | |
| Long-Axis Diameter (cm) | 3.92±0.08 | 4.00±0.09 | 4.09±0.12 | 4.10±0.05 | 4.36±0.06$^{\dagger}$ |
| Short-Axis Diameter (cm) | 2.55±0.04 | 2.59±0.04 | 2.64±0.08 | 2.65±0.05 | 2.68±0.03 |
| Ablation Volume ($cm^3$) | 11.62±0.24 | 12.07±0.1$^{*}$ | 13.25±0.3$^{*}$ | 14.12±0.18$^{*}$ | 15.07±0.4$^{*}$ |
| **Results in *Tumor Informed* Digital Twin** | | | | | |
| Long Axis-Diameter (cm) | 4.01±0.11 | 4.01±0.12 | 4.02±0.11 | 4.03±0.09 | 4.04±0.08 |
| Short Axis-Diameter (cm) | 2.44±0.04 | 2.51±0.06 | 2.83±0.02$^{**,\dagger}$ | 3.03±0.02$^{**,\dagger}$ | 3.10±0.05$^{*,\dagger}$ |
| Ablation Volume ($cm^3$) | 11.27±0.22 | 11.86±0.3$^{*}$ | 14.22±0.2$^{*,\dagger}$ | 16.33±0.4$^{*,\dagger}$ | 17.48±0.6$^{*,\dagger}$ |

***P<.05 **P<.01**

**reports a greater metric when compared to the corresponding metric of the preceding, lower fat content**

**† = P<.01**

**reports a greater metric when compared to the corresponding metric within the same fat content between digital twins**

*Tumor Informed DTs*) significantly increased ablation volumes in mild-, moderate-, and high-fat liver content. Furthermore, the long-axis ablation diameter was significantly larger in high-fat tissues for *Tumor Naïve DTs*, whereas *Tumor Informed DTs* exhibited significantly larger short-axis diameters in tissues with mild-, moderate-, and high-fat content.

Fig. 8 displays the results in the context of varying the four antenna placements, fat content, and the presence of tumor-specific properties explicitly modeled for the 2450 MHz ablations. When ranking each position based on ablated tissue among all fat contents, *A* resulted in the most tissue damage, followed by *D*, *B*, and *C*. When comparing the ablation of surrounding tissue vs. tumor tissue, approximately 8.9–10.7 $cm^3$ and 8.8–11.3 $cm^3$ (or 70–90% and 80–95%) of ablated tissue was tumor tissue in *Tumor Naïve* and *Tumor Informed DTs*, respectively.

Fig. 9 visualizes the signed distance to agreement ($SDA_{A\text{-}T}$) between the boundary points of the final ablation volume (time = 15 minutes) and tumor accompanied by the ($SDA_{T\text{-}A}$) between the edges of the tumor and the boundary points (BPs) in high-fat livers with the 2450 MHz antenna. The $SDA_{A\text{-}T}$ distributions are similar between the *Tumor Naïve* and the *Tumor Informed DTs*, with slight distinctions in *A*, *B*, and *D*. Across all placement strategies, the maximum $SDA_{A\text{-}T}$ is between 7–15 mm in both *Tumor Naïve* and *Tumor Informed DTs*. A distinction was reported for placements *A*, *C*, and *D,* where the maximum $SDA_{A\text{-}T}$ was lower in *Tumor Informed* (<12 mm) than *Tumor Naïve DTs* (>13 mm). The $SDA_{T\text{-}A}$ of the *Tumor Naïve DTs* exhibit adequate ablation coverage in the medial portion of the tumor but decreased coverage in the superior and inferior regions. *Tumor Informed* DTs demonstrated near total ablation coverage of the superior and medial portion of the tumor, with reduced coverage in the inferior region. Both highlighted that the irregularly shaped superior tumor border and elongated inferior portions were particularly challenging portions to ablate across all placements.

## IV. DISCUSSION

### A. Effects of Fat

The fundamental advances between this work and previous efforts are the inclusion of temperature-dependent material properties and the spatial encoding of tumor-heterogeneous material properties from mDIXON imaging to create *Tumor Informed* DTs. Previous research demonstrated that elevated fat content within tissue leads to increased ablation volume predictions, compared to tissue with lower fat concentrations [43], [49]. Previous studies also established that elevated intrahepatic fat acts as an insulative barrier that enables power deposition at locations farther from the antenna leading to increased ablation volumes, i.e., the so-called "oven effect" often noted clinically [73], [74]. However, unlike those studies, the influence of the tumor and its fat presentation determined by mDIXON imaging was investigated, and, in some instances (e.g., Table IV (†)), significant differences between ablation performance with and without the presence of the tumor were demonstrated. While our simulation environment enabled us to explore a range of scenarios of tumor- and parenchyma-presented fat distributions, it should be noted that the mDIXON imaging that informed the heterogeneous model of Fig. 4 did represent a 2:1 difference in fat content when comparing parenchyma to tumor, suggesting that substantial differences can be present. A notable finding in this work is that the relative shape and size of the ablation volumes were consistent within each steatosis grade across antennae placements. It is also important to recognize that applying the long and short-axis diameters to calculate ellipsoid ablation volumes can produce discrepancies to the true ablation volume. Ablation volumes have been recognized as irregular shapes but are clinically characterized using Feret measurements, i.e., largest diameter lengths. While they are necessary measurements, they are recognized as approximations [68], [75], [76].

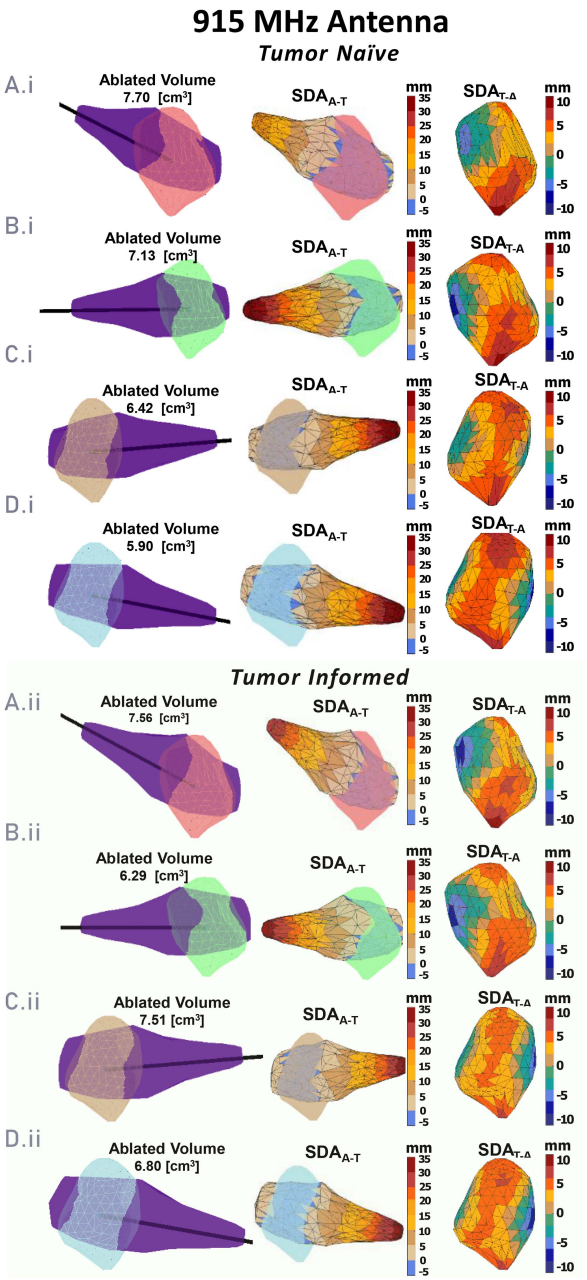


**Fig. 7.** Two signed distance to agreements, $SDA_{A\text{-}T}$ and $SDA_{T\text{-}A}$ between the boundary points (BPs) of the final ablation volume and the edges of the tumor in high-fat livers (915 MHz antenna, 15 minutes at 60 W power). Ablation volumes from high-fat models were selected to illustrate the maximum ablation coverage possible. Positive $SDA_{A\text{-}T}$ values indicate extra-tumoral ablation margins, i.e., surrounding tissue damage, while negative values indicate ablated tumor. Positive $SDA_{T\text{-}A}$ indicate regions of incomplete tumor ablation and negative values indicate regions of ablated tumor. The tumor is oriented to highlight areas in regions with less ablation coverage, and placements A-D are labeled for (i) *Tumor Naïve* and (ii) *Tumor Informed* digital twins.

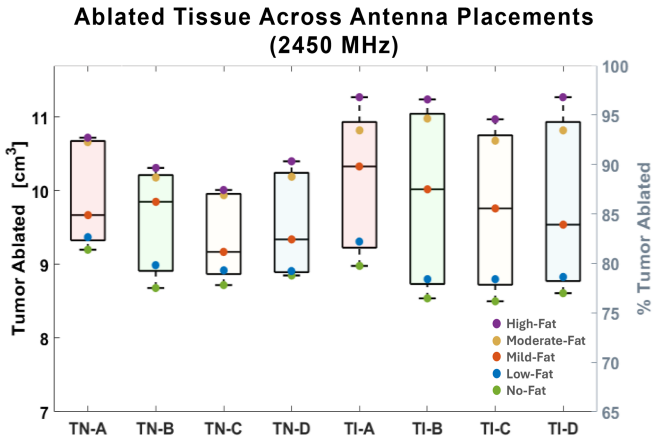


**Fig. 8.** Boxplot of the final tumor ablated volume ($cm^3$) and percent (%) tumor ablated (2450 MHz antenna, 15 minutes at 60 W power) across all fat contents and antenna placements (A-D) in *Tumor Naïve* (TN) and *Tumor Informed* (TI) digital twins. Original tumor volume is 11.7 $cm^3$. Fig. 8 Boxplot of the final tumor ablated volume ($cm^3$) (2450 MHz antenna, 15 minutes at 60 W power) across all fat contents and antenna placements (A-D) in *Tumor Naïve* (TN) and *Tumor Informed* (TI) digital twins.

It is interesting to consider the role of fat in digital twin prediction. Previous work demonstrated that distributed fatty liver disease in the parenchyma could be represented by its average. Herein, mDIXON analysis demonstrated that intra-tumoral fat levels can differ from that of the parenchyma (Table I). This suggests that in the presence of focal deposits of different fat expressions that are in the near-field of the antenna, ablation predictions could be different. While the study presented here did not specifically investigate focal fatty liver disease effects, the results are suggestive, and further study of fat fraction presentation (intra-tumoral fat, and focal disease) occurring with primary and metastatic patients is warranted among patients who are candidates for locoregional therapies.

### B. Targeting With the 915 MHz Antenna

In the 915 MHz antenna simulations, the final tumor ablated volumes increased by ∼42% and ∼60% from no-fat to high-fat content in the *Tumor Naïve* and *Tumor Informed DTs*, respectively (Table III). Paired *t*-tests did not find significant differences in ablation volume predictions in the presence of tumor-specific properties. A similar finding was established in previous work using the same antenna design [43]. Analyzing the results from Fig. 6, approximately 50–65% of the total ablated tissue was tumor, across all antenna orientations. As evidenced in Fig. 7, while both the ablation and tumor are ellipsoidal, the challenging location and size of the tumor are not optimal for this antenna type. Furthermore, Fig. 7 indicates that when the ablation volume prediction is maximized, placement *A* produces the greatest tumor coverage in the upper and lower portions. A promising aspect of these results is that the mean and standard deviation of the ablation volume revealed that antenna orientation had a negligible effect on the predicted ablation volume (Table III). This is likely attributed to the antenna design and microwave frequency, and suggests that this antenna could be applied to adaptive targeting strategies to ablate large or nodular tumors [77]. Overall, while the results of the *Tumor Informed* and *Tumor Naïve* DTs reveal that tumor properties do not significantly affect ablation margins, this analysis is crucial for understanding the effects and limitations of this specific probe design (single-slot 915 MHz probe). Considering the

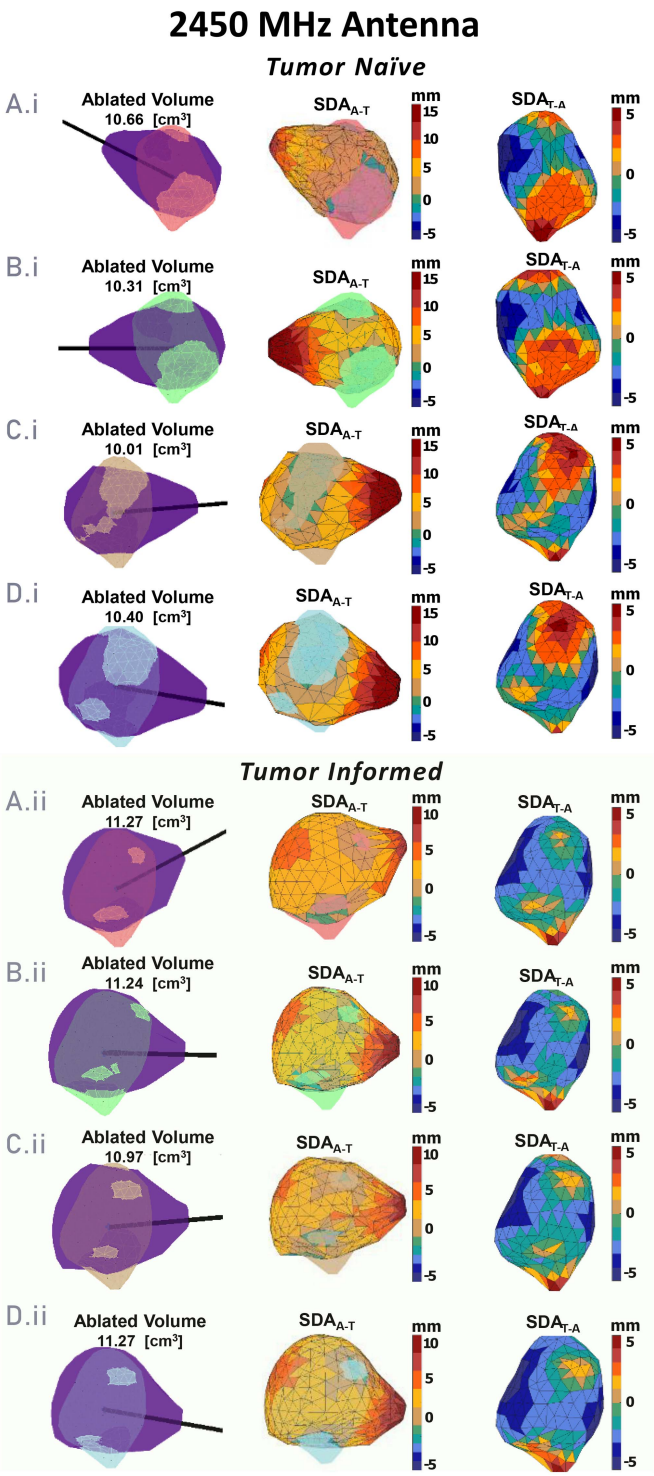


**Fig. 9.** Two signed distance to agreements, $SDA_{A\text{-}T}$ and $SDA_{T\text{-}A}$ between the boundary points (BPs) of the final ablation volume and the edges of the tumor in high-fat livers (2450 MHz antenna, 15 minutes at 60 W power). Ablation volumes from high-fat models were selected to illustrate the maximum ablation coverage possible. Positive $SDA_{A\text{-}T}$ values indicate extra-tumoral ablation margins, i.e., surrounding tissue damage, while negative values indicate ablated tumor. Positive $SDA_{T\text{-}A}$ values indicate regions of incomplete tumor ablation, and negative values indicate regions of ablated tumor. The tumor is oriented to highlight areas in regions with less ablation coverage, and placements A-D are labeled for (i) *Tumor Naïve* and (ii) *Tumor Informed* digital twins.

various 915 MHz probe designs, it is unclear whether tumor properties significantly affect ablation margins at this frequency.

### C. Targeting With the 2450 MHz Antenna

In the 2450 MHz antenna simulations, Table IV reports final tumor ablated volumes increased by approximately 29% and 55% from no-fat to high-fat in the *Tumor Naïve* and *Tumor Informed DTs*, respectively. Furthermore, the presence of tumor increased ablation volume predictions within steatosis grades, and produced more spherical ablations compared to the 915 MHz antenna, as illustrated in Table IV, Figs. 9, and 7 The results in Fig. 9 report that approximately 65–80% and 60–80% of total tissue ablated was the tumor in the *Tumor Naïve* and *Tumor Informed DTs*, respectively. This marks a substantial performance increase when compared to the 915 MHz antenna, which was an anticipated outcome considering that the tumor has an approximate sphericity of 0.74, which is closer to the sphericity of the 2450 MHz ablations than the 915 MHz ablations (0.6–0.75 vs. 0.25–0.30, respectively). Additionally, it is well established that 2450 MHz antennae result in larger and more spherical ablation margins at a similar thermal dose compared to 915 MHz [34], [63], [64]. Furthermore, similarly to the 915 MHz antenna, neither digital twin could completely ablate the lower or upper half of the tumor.

As per the established protocol for MWA ablation therapy, all antennas were directed toward the center of the tumor to maximize ablation efficacy [7]. It is clear that neither antenna at this particular thermal dose can envelop the entire tumor. While the 2450 MHz probe has increased coverage, it is also noted that extra-tumoral parenchyma is becoming increasingly involved. While over-ablation into surrounding parenchyma is not typically a problem, nearby high-risk structures such as bile ducts and extrahepatic anatomy may need to be considered in other tumor presentations as surrounding tissue is increasingly impacted [78]. Conventionally, MWA is not considered overly conformal, hence the guidelines of favorable outcomes when treating tumors less than 3 cm [7], [79]. However, if the therapy is to extend beyond these constraints, more conformal delivery with improved planning, varying frequency, and antenna design is a pressing need.

In addition, there is growing interest in developing targeting strategies that maximize tumor destruction in the context of combination therapies. One of the reported challenges of partial ablation for combination therapy is to maximize tumor destruction while controlling tumor remnants [61]. For example, microwave ablation can be followed with transarterial chemoembolization (TACE) to destroy tumor remnants but requires vasculature near the tumor remnant to be preserved for the administration of chemotherapeutic agents [80], [81], [82]. Poorly planned ablations could complicate this procedure by occluding small vasculature, which could interfere with TACE delivery [83], [84]. Another recent strategy is the simultaneous application of multiple antennae to ablate large tumors while still preserving surrounding tissue [85], [86], [87]. In future work, developing targeting strategies to steer the ablation zone towards distal tissue

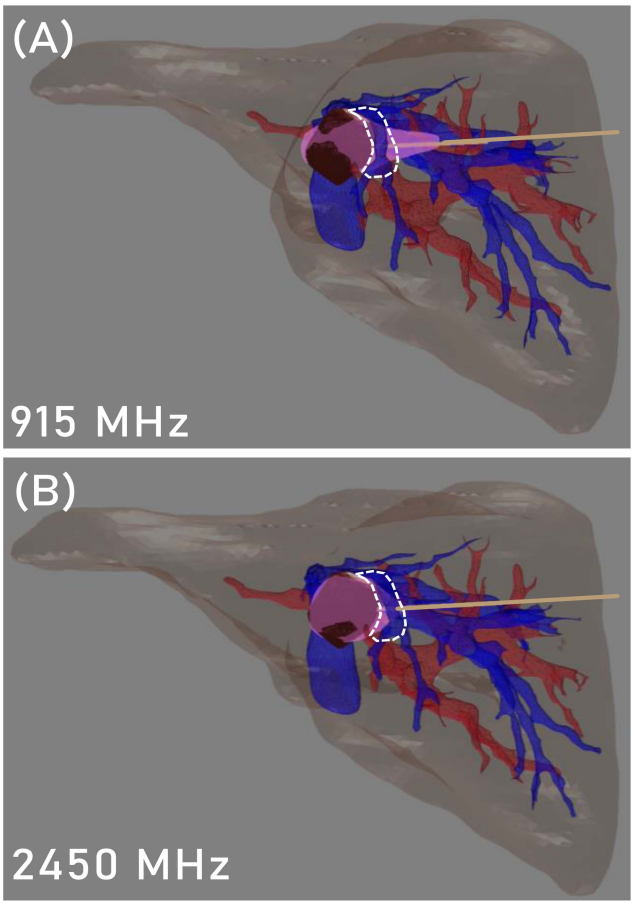


**Fig. 10.** Microwave ablation volume in a high-fat *Tumor Informed Digital Twin* using a 915 MHz antenna (a) and a 2450 MHz antenna (b) in antenna placement C. The region of overlap between the ablation volume and the right hepatic vein is highlighted in a white outline.

while preserving vasculature to focus on controlling the tumor remnant would be intriguing [88], [89].

### *D. Analysis of Ablation Margin Extent to Surrounding Tissue*

In this study, tumor coverage and ablation margin extent are described using a 0 mm tumor margin to analyze topographical features. In clinical practice, it is recommended to ablate 5–10 mm beyond the tumor as a 'safety margin' [7], [90]. Figs. 7 and 8. visualize the signed distance to agreement between the tumor and ablation volume ($SDA_{A\text{-}T}$) for the 915 MHz and 2450 MHz antennae, respectively. This signed distance calculation is necessary for understanding the ablation boundary's extent outside the tumor. Ablation extent and tumor coverage were illustrated by calculating $SDA_{A\text{-}T}$ and $SDA_{T\text{-}A}$, respectively, which were then annotated on the tumor mesh. Analysis of the 915 MHz antenna data showed that all digital twins had an $SDA_{A\text{-}T} >$ 25mm, which can indicate consequential damage to surrounding tissue, especially when considering the tumor's proximity to the surface of the liver and nearby vasculature (Fig 10(a)). Furthermore, calculating the average surrounding tissue damage across all antennae placements in *both Tumor Naïve* and *Tumor Informed DTs* revealed that no-, low-, mild-, moderate-, and high-fat models had a volumetric damage of 3.15 $cm^3$, 3.74 $cm^3$, 4.23 $cm^3$, 4.71 $cm^3$, and 5.99 $cm^3$, respectively. One placement strategy criterion is that the antenna trajectory navigated around vasculature, corresponding with clinical practice, yet when visualizing the largest ablation volume for each placement (high-fat at 15 minutes) along with all the liver structures, there was partial overlap with the right hepatic vein in placements A, B, and C (Fig. 10(a)), likely due to the fact that the ablation volume was not yet known [7], [91], [92]. Although some have reported that transthoracic ablation can be safe, it is not considered favorable [93]. With this context, intuitively, placement *D* would appear to be the safest and most accessible route but was compromised by having the lowest tumor ablation characteristics.

In the 2450 MHz antenna, Fig. 9 illustrates that all digital twins had an $SDA_{A\text{-}T} <$15 mm, which is an improvement, but the distribution reveals that the majority of the boundary points were outside of the tumor, which would indicate a greater degree of surrounding tissue damage; However, when visualizing the data again, there was minimal overlap with the right hepatic vein (Fig. 10(b)). Figs. 6 and 8 provide precise measurements of tumor coverage, which is a primary concern due to the tumor's location, and by extension damage to surrounding tissue, both of which are crucial for intraprocedural planning and navigation. Upon closer inspection, calculating the average surrounding tissue damage across all antennae placements strategies in *Tumor Naïve DTs* revealed that no-, low-, mild-, moderate-, and high-fat models had 2.76 $cm^3$, 3.02 $cm^3$, 3.74 $cm^3$, 3.88 $cm^3$, and 4.71 $cm^3$ volumetric damage, respectively. Correspondingly, surrounding tissue damage in *Tumor Informed DTs,* no-, low-, mild-, moderate-, and high-fat models had 2.61 $cm^3$, 2.92 $cm^3$, 4.31 $cm^3$, 5.51 $cm^3$, and 6.29 $cm^3$ respectively.

If signed distance to agreement were to be applied as a metric for a guidance system, the signed distance between the tumor and ablation volume ($SDA_{T\text{-}A}$) should be used to preoperatively interrogate tumor coverage in the context of whole tumor ablation or complete ablation of tumor regions [90]. Achieving a successful ablation and avoiding residual tumor tissue or recurrence depends on maintaining an adequate safety margin [79], [94], [95]. While there is no universal agreement on the exact distance, most experts suggest a margin of 5–10 mm [96]. As shown in Figs. 7 and 9, this use of signed distance to agreement is similar to how Intensity Modulated Radiotherapy is planned and evaluated to achieve total tumor coverage [97], [98], [99]. Additionally, the signed distance between the ablation volume and the tumor ($SDA_{A\text{-}T}$) should be minimized to control surrounding tissue destruction. A paper by Groves et al. describes using signed distance as a performance metric for needle insertion in mixed reality applications using similar principles described herein [100]. The specific ablation visualizations of ablation coverage presented Figs. 7 and 9 would be adapted for use in planning to prioritize the view of the ablation volume and the tumor, but it would be valuable to provide annotated signed distance information as an optional mode. In addition to these metrics, selecting a trajectory that avoids large vasculature (>1 cm in diameter) should also be considered when possible. In application, it would be feasible to integrate these methods in

an image-guided therapy platform, like the Cas-One IR system (CASCINATION, Bern, Switzerland), or a customized surgical guidance system based on existing open-source software such as 3D Slicer [101], [102], [103].

### E. Limitations

One limitation of the work is the availability of fat quantification imaging within the context of MWA and locoregional therapy. In this work, fat quantification scans were acquired in the context of routine surveillance or diagnostic workup. An extensive understanding of these biomarkers is a pressing problem and is somewhat under-investigated. As background, tumors in previous work established tumor permittivity, thermal and electrical conductivity to be approximately 19%, 16%, and 44%, greater than liver parenchyma, respectively [65], [66]. For the simulations reported herein, the relationship mapping liver parenchyma material properties was based on experimental work within mock tissue phantom studies that utilized fat content as a surrogate. The reality is that an in vivo understanding of these biomarkers is currently unavailable [37], [65]. Because the model directly adapted work from Silva et al., the study did not include constitutive models to capture the effects of temperature on dielectric properties and in the future it would be valuable to include these relationships in a custom ablation model [26], [29], [104]. Additionally, we have not modeled certain local phenomena, such as triglyceride melting above 65 °C or tissue contracting from water loss, which can potentially affect the appearance of postoperative ablation [105], [106]. Additionally, the local effects of large vessel perfusion nor the effects of heat were not modeled, and although the antennae tip was placed ∼2 cm away from large vessels, literature data suggest that the peripheral margins of the ablation zone near large vessels would be reduced [8], [26]. Work in radiofrequency suggests that the coagulation produced by ablation zones close blood vessels and can ultimately reduce local perfusion [107].

The work in this paper was based on a presentation where the tumor average fat fraction was approximately 5.56% while the surrounding parenchyma was approximately 12.7%. This distribution indicates an "oven effect" phenomenon that has been noted clinically and aligns well with physician experiences. Previous work indicates that the presence of more conductive tumors lead to larger ablation volumes. [74], [108]. In tissue analyses, like those performed by O'Rourke et al. and Shetty et al., it was observed that tumors had higher conductivity than the surrounding liver, but supportive data is limited [65], [109]. Ultimately, extensive patient sampling is necessary to better understand presentations, particularly in the context of emerging pathophysiologies such as NAFLD.

As exemplified here, material property values that spanned low-, moderate-, and high-fat livers were used for the parenchyma, while tumor fat content presentation values were mapped from patient data. From Table I, the liver parenchyma of the no- and low-fat contents are more conductive than the tumor in these cases, which consequently did not produce the oven effect. The predicted ablation volumes in the *Tumor Informed DTs* were smaller than the *Tumor Naïve* DTs, which deviates from previous work [43]. Contrarily, the parenchyma of the *Tumor Informed* DTs for mild-, moderate-, and high-fat content was less conductive than the tumor in these presentations. These observations would represent conditions where the "oven effect" likely increases predicted ablation volumes (Tables III and IV).

The current framework reported herein was designed to thoroughly process and create a high-quality investigative computational model. Using this strategy would require approximately 7-8 hours for a placement strategy to be simulated—from the time a patient is imaged to a complete ablation analysis (Fig. 1**).** In this work, the whole liver and the vasculature were carefully, manually segmented in 4-6 hours (Fig. 1(a) and (d)). The computational model is predeveloped beforehand, and only the tumor and liver mesh and material property data, which are generated using customized algorithms, are required to be imported. The duration of the simulation is dependent on the duration of the ablation, which was, on average, 3.5 hours. Finally, data post-processing is streamlined with custom code, which takes 15 minutes to process and visualize. The desktop computer used in this study has the following specifications: 64-bit Windows 10, AMD 78-core 3593 MHz processor, 48 GBs of RAM, and an NVIDIA GeForce RTX 2060 graphics card with 6 GB VRAM.

The two primary limitations of this framework are the segmentation of the liver and vessels and the finite element models. Reducing the segmentation time would be feasible if using semi-automatic techniques instead of manual work. Currently, algorithms exist to segment whole livers and large vessels in magnetic quantification images- which can significantly reduce manual effort [110], [111], [112]. The finite element simulations require the most computational resources to forecast one antennae configuration. Because of the model's complexity, there are no alternatives to replicating the results with other methods. Fortunately, there is emerging machine learning research towards replicating finite element simulations using time-varying networks. However, these these networks require existing simulation work to accurately forecast [113].

The exploration conducted within this manuscript is intriguing. While conventional MWA therapy has patient stratification constraints that limit its use to what is perceived as the most efficacious use, these decisions limit the deployment of the technology due to a lack of perceived controllability [76], [114]. The digital twin model presented in this work is considered a tool of discovery, where the goal is to comprehensively document the effects of tissue composition on forecasted ablation volumes. An important extension of this work would be to explore power configurations beyond 60W to explore the differences in ablation coverage within and between antennae models. Additionally, the analysis of the digital twins also serves as a platform for developing strategies that would enable better predictability in clinical practice.

Overall, the investigation here suggests that healthcare digital twin approaches combined with novel antenna designs, combination therapies, or multiple probe ablations may be essential in moving MWA to a more conformal therapy that could be used in a wider range of indications.

## V. Conclusion

Ablation is employed as a curative treatment for early-stage clinical presentations of hepatic cancer and has taken on a critical role in disease management to bridge patients to transplant, improve quality of life, and contribute to novel combination therapies [88], [89], [115]. Additionally, the incidence and complications of liver cancer have been observed to be exacerbated by metabolic disorders associated with an evolving disease population, namely, the increasing incidences of cancer with NAFLD [2], [3], [7], [38]. This study presents a transformative concept for employing image-based biomarkers to enhance patient specificity, interventional planning, and treatment delivery in relation to fatty liver disease. Additionally, the illuminating landscape on relevant liver-based biomarker imaging modalities such as fat quantification, perfusion, elastography, etc., promotes captivating possibilities in promoting a more conformal patient-specific delivery of thermal therapies [116], [117], [118]. The ability to link quantitative and anatomical imaging to develop navigational strategies and evaluate the performance of therapeutic delivery is critical when considering the adaptation of therapies in the context of an evolving disease and an attempt to increase indications for The use of MWA. The work herein reinforces the importance of utilizing quantitative imaging biomarkers to tailor treatments to individual patients, which may be instrumental in improving patient outcomes and accommodating the dynamic nature of disease progression.

## Author Contributions

The authors would like to thank the study participants for their support of this study through their generous participation. We thank the research team (Dr. Jarrod A. Collins & Dr. Michael I. Miga) who helped develop the digital twin biophysical model,

the study personnel at MSKCC (Dr. Jon S. Heiselman & Dr. William R. Jarnagin) who for their recruitment and processing of study participants, and personnel at VUMC (Dr. Virginia B. Planz, Dr. Daniel B. Brown, Dr. Sunil K. Geevarghese, and Dr. Katherine C. Frederick-Dyer) for guiding the clinical approach and applications of the digital twin for microwave ablation therapy.

*Conflict of Interest:* We have no conflicts of interest to disclose.

## References

[1] R. L. Siegel, K. D. Miller, N. S. Wagle, and A. Jemal, "Cancer statistics, 2023," *CA: A Cancer J. Clinicians*, vol. 73, no. 1, pp. 17–48, 2023, doi: 10.3322/caac.21763.

[2] A. K. Singh, R. Kumar, and A. K. Pandey, "Hepatocellular carcinoma: Causes, mechanism of progression and biomarkers," *Curr. Chem. Genomic. Transl. Med.*, vol. 12, pp. 9–26, Jun. 2018, doi: 10.2174/2213988501812010009.

[3] R. Masuzaki, S. J. Karp, and M. Omata, "NAFLD as a risk factor for HCC: New rules of engagement?," *Hepatol. Int.*, vol. 10, no. 4, pp. 533–534, May 2016, doi: 10.1007/s12072-016-9731-8.

[4] A. B. Couillard et al., "Microwave ablation as bridging to liver transplant for patients with hepatocellular carcinoma: A single-center retrospective analysis," *J. Vasc. Interventional Radiol.*, vol. 33, no. 9, pp. 1045–1053, Sep. 2022, doi: 10.1016/j.jvir.2022.05.019.

[5] C. Fang et al., "Complications from percutaneous microwave ablation of liver tumours: A pictorial review," *Brit. J. Radiol.*, vol. 92, no. 1099, Jul. 2019, Art. no. 20180864, doi: 10.1259/bjr.20180864.

[6] C. C. Jadlowiec and T. Taner, "Liver transplantation: Current status and challenges," *World J. Gastroenterol.*, vol. 22, no. 18, pp. 4438–4445, May 2016, doi: 10.3748/wjg.v22.i18.4438.

[7] A. B. Benson et al., "Hepatobiliary cancers, version 2.2021, NCCN clinical practice guidelines in oncology," *J. Nat. Comprehensive Cancer Netw.*, vol. 19, no. 5, pp. 541–565, May 2021, doi: 10.6004/jnccn.2021.0022.

[8] M. G. Lubner, C. L. Brace, J. L. Hinshaw, and F. T. Lee, "Microwave tumor ablation: Mechanism of action, clinical results and devices," *J. Vasc. Interventional Radiol.*, vol. 21, no. 8, pp. S192–S203, Aug. 2010, doi: 10.1016/j.jvir.2010.04.007.

[9] T. Shibata et al., "Small hepatocellular carcinoma: Comparison of radiofrequency ablation and percutaneous microwave coagulation therapy," *Radiology*, vol. 223, no. 2, pp. 331–337, May 2002, doi: 10.1148/radiol.2232010775.

[10] J. Shi et al., "Comparison of microwave ablation and surgical resection for treatment of hepatocellular carcinomas conforming to Milan criteria," *J. Gastroenterol. Hepatol.*, vol. 29, no. 7, pp. 1500–1507, 2014, doi: 10.1111/jgh.12572.

[11] M. Reig et al., "Diagnosis and treatment of hepatocellular carcinoma. update of the consensus document of the AEEH, AEC, SEOM, SERAM, SERVEI, and SETH," *Medicina Clinica*, vol. 156, no. 9, pp. 463.e1–463.e30, May 2021, doi: 10.1016/j.medcli.2020.09.022.

[12] B. Radjenović, M. Sabo, L. Šoltes, M. Prnova, P. Čičak, and M. Radmilović-Radjenović, "On efficacy of microwave ablation in the thermal treatment of an early-stage hepatocellular carcinoma," *Cancers*, vol. 13, no. 22, Nov. 2021, Art. no. 5784, doi: 10.3390/cancers13225784.

[13] J. Sebek, S. Curto, R. Bortel, and P. Prakash, "Analysis of minimally invasive directional antennas for microwave tissue ablation," *Int. J. Hyperthermia*, vol. 33, no. 1, pp. 51–60, Jan. 2017, doi: 10.1080/02656736.2016.1195519.

[14] B. T. McWilliams, E. E. Schnell, S. Curto, T. M. Fahrbach, and P. Prakash, "A directional interstitial antenna for microwave tissue ablation: Theoretical and experimental investigation," *IEEE Trans. Biomed. Eng.*, vol. 62, no. 9, pp. 2144–2150, Sep. 2015, doi: 10.1109/TBME.2015.2413672.

[15] W. K. C. Park et al., "The in vivo performance of a novel thermal accelerant agent used for augmentation of microwave energy delivery within biologic tissues during image-guided thermal ablation: A porcine study," *Int. J. Hyperthermia*, vol. 34, no. 1, pp. 11–18, Feb. 2018, doi: 10.1080/02656736.2017.1317367.

[16] A. W. P. Maxwell, W. K. C. Park, G. L. Baird, D. W. Martin, K. A. Lombardo, and D. E. Dupuy, "Effects of a thermal accelerant gel on microwave ablation zone volumes in lung: A porcine study," *Radiology*, vol. 291, no. 2, pp. 504–510, May 2019, doi: 10.1148/radiol.2019181652.

[17] A. W. P. Maxwell, W. K. C. Park, G. L. Baird, E. G. Walsh, and D. E. Dupuy, "Adjuvant thermal accelerant gel use increases microwave ablation zone temperature in porcine liver as measured by MR thermometry," *J. Vasc. Interventional Radiol.*, vol. 31, no. 8, pp. 1357–1364, Aug. 2020, doi: 10.1016/j.jvir.2020.01.010.

[18] J. M. Llovet et al., "Nonalcoholic steatohepatitis-related hepatocellular carcinoma: Pathogenesis and treatment," *Nature Rev. Gastroenterol. Hepatol.*, vol. 20, no. 8, pp. 487–503, Aug. 2023, doi: 10.1038/s41575-023-00754-7.

[19] T. Erol, A. F. Mendi, and D. Doğan, "The digital twin revolution in healthcare," in *Proc. IEEE 4th Int. Symp. Multidisciplinary Stud. Innov. Technol.*, 2020, pp. 1–7. doi: 10.1109/ISMSIT50672.2020.9255249.

[20] B. Kaufmann, A. Reca, B. Wang, H. Friess, A. E. Feldstein, and D. Hartmann, "Mechanisms of nonalcoholic fatty liver disease and implications for surgery," *Langenbeck's Arch. Surg.*, vol. 406, no. 1, pp. 1–17, Feb. 2021, doi: 10.1007/s00423-020-01965-1.

[21] W. A. Curtis, T. J. Fraum, H. An, Y. Chen, A. S. Shetty, and K. J. Fowler, "Quantitative MRI of diffuse liver disease: Current applications and future directions," *Radiology*, vol. 290, no. 1, pp. 23–30, Jan. 2019, doi: 10.1148/radiol.2018172765.

[22] V. Bhat, S. Velandai, V. Belliappa, J. Illayraja, K. G. Halli, and G. Gopalakrishnan, "Quantification of liver fat with mDIXON magnetic resonance imaging, comparison with the computed tomography and the biopsy," *J. Clin. Diagn. Res.*, vol. 11, no. 7, pp. TC06–TC10, Jul. 2017, doi: 10.7860/JCDR/2017/26317.10234.

[23] D. E. Kleiner et al., "Design and validation of a histological scoring system for nonalcoholic fatty liver disease," *Hepatology*, vol. 41, no. 6, pp. 1313–1321, 2005, doi: 10.1002/hep.20701.

[24] I. S. Idilman et al., "Hepatic steatosis: Quantification by proton density fat fraction with MR imaging versus liver biopsy," *Radiology*, vol. 267, no. 3, pp. 767–775, Jun. 2013, doi: 10.1148/radiol.13121360.

[25] A. Tang et al., "Nonalcoholic fatty liver disease: MR imaging of liver proton density fat fraction to assess hepatic steatosis," *Radiology*, vol. 267, no. 2, pp. 422–431, May 2013, doi: 10.1148/radiol.12120896.

[26] G. Deshazer, D. Merck, M. Hagmann, D. E. Dupuy, and P. Prakash, "Physical modeling of microwave ablation zone clinical margin variance," *Med. Phys.*, vol. 43, no. 4, Apr. 2016, Art. no. 1764, doi: 10.1118/1.4942980.

[27] S. R. Guntur, K. I. Lee, D. - G. Paeng, A. J. Coleman, and M. J. Choi, "Temperature-dependent thermal properties of ex vivo liver undergoing thermal ablation," *Ultrasound Med. Biol.*, vol. 39, no. 10, pp. 1771–1784, Oct. 2013, doi: 10.1016/j.ultrasmedbio.2013.04.014.

[28] V. Lopresto, A. Argentieri, R. Pinto, and M. Cavagnaro, "Temperature dependence of thermal properties of ex vivo liver tissue up to ablative temperatures," *Phys. Med. Biol.*, vol. 64, no. 10, May 2019, Art. no. 105016, doi: 10.1088/1361-6560/ab1663.

[29] N. P. Silva, A. Bottiglieri, R. C. Conceição, M. O'Halloran, and L. Farina, "Characterisation of ex vivo liver thermal properties for electromagnetic-based hyperthermic therapies," *Sensors*, vol. 20, no. 10, Jan. 2020, Art. no. 3004, doi: 10.3390/s20103004.

[30] H. B. El–Serag and K. L. Rudolph, "Hepatocellular carcinoma: Epidemiology and molecular carcinogenesis," *Gastroenterology*, vol. 132, no. 7, pp. 2557–2576, Jun. 2007, doi: 10.1053/j.gastro.2007.04.061.

[31] J. M. Llovet et al., "Hepatocellular carcinoma," *Nature Rev. Dis. Primers*, vol. 7, no. 1, pp. 441–445, Jan. 2021, doi: 10.1038/s41572-020-00240-3.

[32] P. Hasgall et al., "IT'IS database for thermal and electromagnetic parameters of biological tissues," *Version 4.1*, 2022, doi: 10.13099/VIP21000-04-1.

[33] A. S. Ashour, M. Asran, and D. I. Fotiadis, "Optimal power for microwave slotted probes in ablating different hepatocellular carcinoma sizes," *Comput. Biol. Med.*, vol. 127, Dec. 2020, Art. no. 104101, doi: 10.1016/j.compbiomed.2020.104101.

[34] K. Cocic, A. Davidovic, and D. L. Sekulic, "Simulation results of 2.45 GHz coaxial antenna with a ring slot for microwave ablation of a cancer," in *Proc. IEEE 31st Int. Conf. Microelectron.*, 2019, pp. 325–328, doi: 10.1109/MIEL.2019.8889592.

[35] H. Gao, X. Wang, S. Wu, Z. Zhou, Y. Bai, and W. Wu, "Conformal coverage of liver tumors by the thermal coagulation zone in 2450-MHz microwave ablation," *Int. J. Hyperthermia*, vol. 36, no. 1, pp. 590–604, Jan. 2019, doi: 10.1080/02656736.2019.1617437.

[36] M. H. H. Tehrani, M. Soltani, F. M. Kashkooli, and K. Raahemifar, "Use of microwave ablation for thermal treatment of solid tumors with different shapes and sizes—A computational approach," *PLoS One*, vol. 15, no. 6, Jun. 2020, Art. no. e0233219, doi: 10.1371/journal.pone.0233219.

[37] J. Ampuero and M. Romero-Gomez, "Stratification of patients in NASH clinical trials: A pitfall for trial success," *JHEP Rep.*, vol. 2, no. 5, Oct. 2020, Art. no. 100148, doi: 10.1016/j.jhepr.2020.100148.

[38] M. Arrese, J. P. Arab, F. Barrera, B. Kaufmann, L. Valenti, and A. E. Feldstein, "Insights into nonalcoholic fatty-liver disease heterogeneity," *Seminars Liver Dis.*, vol. 41, no. 4, pp. 421–434, Nov. 2021, doi: 10.1055/s-0041-1730927.

[39] O. Cheung et al., "The impact of fat distribution on the severity of nonalcoholic fatty liver disease and metabolic syndrome," *Hepatology*, vol. 46, no. 4, pp. 1091–1100, 2007, doi: 10.1002/hep.21803.

[40] P. Armeni, I. Polat, L. M. De Rossi, L. Diaferia, S. Meregalli, and A. Gatti, "Digital twins in healthcare: Is it the beginning of a new era of evidence-based medicine? a critical review," *J. Pers. Med.*, vol. 12, no. 8, Jul. 2022, Art. no. 1255, doi: 10.3390/jpm12081255.

[41] M. Liu, S. Fang, H. Dong, and C. Xu, "Review of digital twin about concepts, technologies, and industrial applications," *J. Manuf. Syst.*, vol. 58, pp. 346–361, Jan. 2021, doi: 10.1016/j.jmsy.2020.06.017.

[42] T. Sun, X. He, X. Song, L. Shu, and Z. Li, "The digital twin in medicine: A key to the future of healthcare?," *Front. Med.*, vol. 9, Jul. 2022, Art. no. 907066, doi: 10.3389/fmed.2022.907066.

[43] F. Servin et al., "Fat quantification imaging and biophysical modeling for patient-specific forecasting of microwave ablation therapy," *Front. Physiol.*, vol. 12, 2022, Art. no. 25425. [Online]. Available: https://www.frontiersin.org/article/10.3389/fphys.2021.820251

[44] H. Eggers, B. Brendel, A. Duijndam, and G. Herigault, "Dual-echo dixon imaging with flexible choice of echo times," *Magn. Reson. Med.*, vol. 65, no. 1, pp. 96–107, Jan. 2011, doi: 10.1002/mrm.22578.

[45] B. Henninger et al., "Performance of different Dixon-based methods for MR liver iron assessment in comparison to a biopsy-validated R2∗ relaxometry method," *Eur. Radiol.*, vol. 31, no. 4, pp. 2252–2262, Apr. 2021, doi: 10.1007/s00330-020-07291-w.

[46] S. B. Reeder and C. Sirlin, "Quantification of liver fat with magnetic resonance imaging," *Magn. Reson. Imag. Clin. North Amer.*, vol. 18, no. 3, pp. 337–357, Aug. 2010, doi: 10.1016/j.mric.2010.08.013.

[47] F. Servin et al., "Digital twin forecasting of microwave ablation via fat quantification image-to-grid computational methods," *Proc.SPIE*, vol. 12466, pp. 292–298, 2023, doi: 10.1117/12.2655257.

[48] J. A. Collins, J. S. Heiselman, L. W. Clements, D. B. Brown, and M. I. Miga, "Multiphysics modeling toward enhanced guidance in hepatic microwave ablation: A preliminary framework," *J. Med. Imag.*, vol. 6, no. 2, Apr. 2019, Art. no. 025007, doi: 10.1117/1.JMI.6.2.025007.

[49] J. A. Collins, J. S. Heiselman, L. W. Clements, J. A. Weis, D. B. Brown, and M. I. Miga, "Toward image data-driven predictive modeling for guiding thermal ablative therapy," *IEEE Trans. Biomed. Eng.*, vol. 67, no. 6, pp. 1548–1557, Jun. 2020, doi: 10.1109/TBME.2019.2939686.

[50] D. Kernot et al., "Transient changes during microwave ablation simulation : A comparative shape analysis," *Biomech. Model. Mechanobiol.*, vol. 22, no. 1, pp. 271–280, Feb. 2023, doi: 10.1007/s10237-022-01646-6.

[51] J. Collins, "Enhanced treatment planning and navigation for image-guided microwave ablation of hepatic tumors," Dec. 15, 2018. Accessed: Oct. 06, 2023. [Online]. Available: https://ir.vanderbilt.edu/handle/1803/14478

[52] F. C. Henriques, "Studies of thermal injury; the predictability and the significance of thermally induced rate processes leading to irreversible epidermal injury," *Arch. Pathol.*, vol. 43, no. 5, pp. 489–502, May 1947.

[53] C. Gabriel, S. Gabriel, and E. Corthout, "The dielectric properties of biological tissues: I. Literature survey," *Phys. Med. Biol.*, vol. 41, no. 11, pp. 2231–2249, Nov. 1996, doi: 10.1088/0031-9155/41/11/001.

[54] P. Prakash and C. J. Diederich, "Considerations for theoretical modeling of thermal ablation with catheter-based ultrasonic sources: Implications for treatment planning, monitoring and control," *Int. J. Hyperthermia*, vol. 28, no. 1, pp. 69–86, 2012, doi: 10.3109/02656736.2011.630337.

[55] W. C. Dewey, "Arrhenius relationships from the molecule and cell to the clinic," *Int. J. Hyperthermia*, vol. 25, no. 1, pp. 3–20, Jan. 2009, doi: 10.1080/02656730902747919.

[56] J. A. Pearce, "Relationship between Arrhenius models of thermal damage and the CEM 43 thermal dose," *Proc. SPIE*, vol. 7181, 2009, Art. no. 718104, doi: 10.1117/12.807999.

[57] S. Siripongsakun, J. K. Lee, S. S. Raman, M. J. Tong, J. Sayre, and D. S. Lu, "MRI detection of intratumoral fat in hepatocellular carcinoma: Potential biomarker for a more favorable prognosis," *Amer. J. Roentgenol.*, vol. 199, no. 5, pp. 1018–1025, Nov. 2012, doi: 10.2214/AJR.12.8632.

[58] S. R. Prasad et al., "Fat-containing lesions of the liver: Radiologic-pathologic correlation," *Radiographics*, vol. 25, no. 2, pp. 321–331, 2005, doi: 10.1148/rg.252045083.

[59] B. E. Van Beers, I. Leconte, R. Materne, A. M. Smith, J. Jamart, and Y. Horsmans, "Hepatic perfusion parameters in chronic liver disease: Dynamic CT measurements correlated with disease severity," *Amer. J. Roentgenol.*, vol. 176, no. 3, pp. 667–673, Mar. 2001, doi: 10.2214/ajr.176.3.1760667.

[60] C. Brace, "Temperature-dependent dielectric properties of liver tissue measured during thermal ablation: Toward an improved numerical model," in *Proc. IEEE 30th Annu. Int. Conf. Eng. Med. Biol. Soc.*, 2008, pp. 230–233, doi: 10.1109/IEMBS.2008.4649132.

[61] Y. Zhou et al., "Challenges facing percutaneous ablation in the treatment of hepatocellular carcinoma: Extension of ablation criteria," *J. Hepatocellular Carcinoma*, vol. 8, pp. 625–644, Jun. 2021, doi: 10.2147/JHC.S298709.

[62] A. Mohammadi, L. Bianchi, S. Asadi, and P. Saccomandi, "Measurement of ex vivo liver, brain and pancreas thermal properties as function of temperature," *Sensors*, vol. 21, no. 12, Jun. 2021, Art. no. 4236, doi: 10.3390/s21124236.

[63] K. A. Simo et al., "Microwave ablation using 915-MHz and 2.45-GHz systems: What are the differences?," *Hepato-Pancreato-Biliary Surg.*, vol. 15, no. 12, pp. 991–996, Dec. 2013, doi: 10.1111/hpb.12081.

[64] S. Curto, M. Taj-Eldin, D. Fairchild, and P. Prakash, "Microwave ablation at 915 MHz vs 2.45 GHz: A theoretical and experimental investigation," *Med. Phys.*, vol. 42, no. 11, pp. 6152–6161, Nov. 2015, doi: 10.1118/1.4931959.

[65] A. P. O'Rourke et al., "Dielectric properties of human normal, malignant and cirrhotic liver tissue: In vivo and ex vivo measurements from 0.5 to 20 GHz using a precision open-ended coaxial probe," *Phys. Med. Biol.*, vol. 52, no. 15, pp. 4707–4719, Aug. 2007, doi: 10.1088/0031-9155/52/15/022.

[66] P. R. Stauffer, F. Rossetto, M. Prakash, D. G. Neuman, and T. Lee, "Phantom and animal tissues for modelling the electrical properties of human liver," *Int. J. Hyperthermia*, vol. 19, no. 1, pp. 89–101, Feb. 2003, doi: 10.1080/0265673021000017064.

[67] J. W. Valvano, J. R. Cochran, and K. R. Diller, "Thermal conductivity and diffusivity of biomaterials measured with self-heated thermistors," *Int. J. Thermophys.*, vol. 6, no. 3, pp. 301–311, May 1985, doi: 10.1007/BF00522151.

[68] F. Michallek et al., "Fractal analysis improves tumour size measurement on computed tomography in pancreatic ductal adenocarcinoma: Comparison with gross pathology and multi-parametric MRI," *Eur. Radiol.*, vol. 32, no. 8, pp. 5053–5063, 2022, doi: 10.1007/s00330-022-08631-8.

[69] K. Samadi and R. S. Arellano, "Microwave ablation of hepatocellular carcinoma metastatic to peritoneum: Diagnostic value of hydrodissection," *Polish J. Radiol.*, vol. 83, pp. e459–e460, Oct. 2018, doi: 10.5114/pjr.2018.80210.

[70] Yury, "Ellipsoid fit - file exchange - MATLAB central," 2015. Accessed: Apr. 19, 2023. [Online]. Available: https://www.mathworks.com/matlabcentral/fileexchange/24693-ellipsoid-fit

[71] J. L. Welsh, K. Bodeker, E. Fallon, S. K. Bhatia, J. M. Buatti, and J. J. Cullen, "Comparison of recist (response evaluation criteria in solid tumors) with volumetric measurements for estimation of tumor burden in pancreatic adenocarcinoma and hepatocellular carcinoma," *Amer. J. Surg.*, vol. 204, no. 5, pp. 580–585, Nov. 2012, doi: 10.1016/j.amjsurg.2012.07.007.

[72] R. Malladi, J. A. Sethian, and B. C. Vemuri, "Shape modeling with front propagation: A level set approach," *IEEE Trans. Pattern Anal. Mach. Intell.*, vol. 17, no. 2, pp. 158–175, Feb. 1995, doi: 10.1109/34.368173.

[73] Z. Liu, M. Ahmed, Y. Weinstein, M. Yi, R. L. Mahajan, and S. N. Goldberg, "Characterization of the RF ablation-induced 'oven effect': The importance of background tissue thermal conductivity on tissue heating," *Int. J. Hyperthermia*, vol. 22, no. 4, pp. 327–342, Jun. 2006, doi: 10.1080/02656730600609122.

[74] T. Livraghi, S. N. Goldberg, S. Lazzaroni, F. Meloni, L. Solbiati, and G. S. Gazelle, "Small hepatocellular carcinoma: Treatment with radio-frequency ablation versus ethanol injection," *Radiology*, vol. 210, no. 3, pp. 655–661, Mar. 1999, doi: 10.1148/radiology.210.3.r99fe40655.

[75] S. J. S. Ruiter, W. J. Heerink, and K. P. de Jong, "Liver microwave ablation: A systematic review of various FDA-approved systems," *Eur. Radiol.*, vol. 29, no. 8, pp. 4026–4035, 2019, doi: 10.1007/s00330-018-5842-z.

[76] S. Young, M. Rivard, R. Kimyon, and T. Sanghvi, "Accuracy of liver ablation zone prediction in a single 2450MHz 100 Watt generator model microwave ablation system: An in human study," *Diagn. Interventional Imag.*, vol. 101, no. 4, pp. 225–233, Apr. 2020, doi: 10.1016/j.diii.2019.10.007.

[77] J. He et al., "The clinicopathologic and prognostic significance of gross classification on solitary hepatocellular carcinoma after hepatectomy," *Medicine*, vol. 94, no. 32, Aug. 2015, Art. no. e1331, doi: 10.1097/MD.0000000000001331.

[78] J. G. Park et al., "Early complications after percutaneous radiofrequency ablation for hepatocellular carcinoma: An analysis of 1,843 ablations in 1,211 patients in a single centre: Experience over 10 years," *Clin. Radiol.*, vol. 72, no. 8, pp. 692.e9–692.e15, Aug. 2017, doi: 10.1016/j.crad.2017.03.001.

[79] P. Gavriilidis, K. J. Roberts, N. de'Angelis, L. Aldrighetti, and R. P. Sutcliffe, "Recurrence and survival following microwave, radiofrequency ablation, and hepatic resection of colorectal liver metastases: A systematic review and network meta-analysis," *Hepatobiliary Pancreatic Dis. Int.*, vol. 20, no. 4, pp. 307–314, Aug. 2021, doi: 10.1016/j.hbpd.2021.05.004.

[80] M. A. A. Basha, "Combined therapy with conventional trans-arterial chemoembolization (cTACE) and microwave ablation (MWA) for hepatocellular carcinoma >3-<5 cm," *Clinicaltrials.gov, Clinical Trial Registration NCT04721470*, Jan. 2021. Accessed: Mar. 12, 2023. [Online]. Available: https://clinicaltrials.gov/ct2/show/NCT04721470

[81] C. Liu, T. Li, J. He, and H. Shao, "TACE combined with microwave ablation therapy vs. TACE alone for treatment of early- and intermediate-stage hepatocellular carcinomas larger than 5 cm: A meta-analysis," *Diagn. Interventional Radiol.*, vol. 26, no. 6, pp. 575–583, Nov. 2020, doi: 10.5152/dir.2020.19615.

[82] F. Weijun, "Effectivity and safety of microwave ablation combined with transcatheter arterial chemoembolization(TACE) for huge unresectable hepatocellular carcinoma: A multicenter analysis," *Clinicaltrials.gov, Clinical Trial Registration NCT03277716*, May 2019. Accessed: Mar. 12, 2023. [Online]. Available: https://clinicaltrials.gov/ct2/show/NCT03277716

[83] J. Chiang et al., "Effects of microwave ablation on arterial and venous vasculature after treatment of hepatocellular carcinoma," *Radiology*, vol. 281, no. 2, pp. 617–624, Nov. 2016, doi: 10.1148/radiol.2016152508.

[84] M. Pleguezuelo et al., "TACE versus TAE as therapy for hepatocellular carcinoma," *Expert Rev. Anticancer Ther.*, vol. 8, no. 10, pp. 1623–1641, Oct. 2008, doi: 10.1586/14737140.8.10.1623.

[85] D. Zhang et al., "Multiple antenna placement in microwave ablation assisted by a three-dimensional fusion image navigation system for hepatocellular carcinoma," *Int. J. Hyperthermia*, vol. 35, no. 1, pp. 122–132, Dec. 2018, doi: 10.1080/02656736.2018.1484183.

[86] C. M. Harari et al., "Microwave ablation: Comparison of simultaneous and sequential activation of multiple antennas in liver model systems," *Radiology*, vol. 278, no. 1, pp. 95–103, Jan. 2016, doi: 10.1148/radiol.2015142151.

[87] T. - Q. Zhang et al., "Sequential and simultaneous 4-antenna microwave ablation in an ex vivo bovine liver model," *Cardiovasc. Interventional Radiol.*, vol. 42, no. 10, pp. 1466–1474, Oct. 2019, doi: 10.1007/s00270-019-02241-6.

[88] C. Roderburg, B. Özdirik, A. Wree, M. Demir, and F. Tacke, "Systemic treatment of hepatocellular carcinoma: From sorafenib to combination therapies," *Hepatic Oncol.*, vol. 7, no. 2, May 2020, Art. no. HEP20, doi: 10.2217/hep-2020-0004.

[89] D. Romero, "Combination set to transform HCC therapy," *Nature Rev. Clin. Oncol.*, vol. 17, no. 7, Jul. 2020, Art. no. 389, doi: 10.1038/s41571-020-0396-9.

[90] R. - M. Sandu et al., "Volumetric quantitative ablation margins for assessment of ablation completeness in thermal ablation of liver tumors," *Front. Oncol.*, vol. 11, Mar. 2021, Art. no. 623098, doi: 10.3389/fonc.2021.623098.

[91] P. Liang et al., "Practice guidelines for ultrasound-guided percutaneous microwave ablation for hepatic malignancy," *World J. Gastroenterol.*, vol. 19, no. 33, pp. 5430–5438, Sep. 2013, doi: 10.3748/wjg.v19.i33.5430.

[92] J. Yu et al., "Local tumour progression after ultrasound-guided microwave ablation of liver malignancies: Risk factors analysis of 2529 tumours," *Eur. Radiol.*, vol. 25, no. 4, pp. 1119–1126, Apr. 2015, doi: 10.1007/s00330-014-3483-4.

[93] H. Qi, H. Zhang, C. Wan, L. Xie, Z. Song, and W. Fan, "CT-guided microwave ablation through the lungs for treating liver tumors near the diaphragm," *Oncotarget*, vol. 8, no. 45, pp. 79270–79278, Apr. 2017, doi: 10.18632/oncotarget.17422.

[94] A. Dupré, R. P. Jones, R. Diaz-Nieto, S. W. Fenwick, G. J. Poston, and H. Z. Malik, "Curative-intent treatment of recurrent colorectal liver metastases: A comparison between ablation and resection," *Eur. J. Surg. Oncol.*, vol. 43, no. 10, pp. 1901–1907, Oct. 2017, doi: 10.1016/j.ejso.2017.08.008.

[95] R. T. Groeschl et al., "Recurrence after microwave ablation of liver malignancies: A single institution experience," *Hepato-Pancreato-Biliary Surg.*, vol. 15, no. 5, pp. 365–371, May 2013, doi: 10.1111/j.1477-2574.2012.00585.x.

[96] J. Schaible et al., "Safety margin assessment after microwave ablation of liver tumors: Inter- and intrareader variability," *Radiol. Oncol.*, vol. 54, no. 1, pp. 57–61, Feb. 2020, doi: 10.2478/raon-2020-0004.

[97] Y. Akino, J. P. Gibbons, D. W. Neck, C. Chu, and I. J. Das, "Intra- and intervariability in beam data commissioning among water phantom scanning systems," *J. Appl. Clin. Med. Phys.*, vol. 15, no. 4, pp. 251–258, 2014, doi: 10.1120/jacmp.v15i4.4850.

[98] R. Avgousti, C. Armpilia, I. Floros, and C. Antypas, "Evaluation of intensity modulated radiation therapy delivery system using a volumetric phantom on the basis of the task group 119 report of American Association of Physicists in Medicine," *J. Med. Phys.*, vol. 42, no. 1, pp. 33–41, 2017, doi: 10.4103/0971-6203.202419.

[99] W. B. Harms, D. A. Low, J. W. Wong, and J. A. Purdy, "A software tool for the quantitative evaluation of 3D dose calculation algorithms," *Med. Phys.*, vol. 25, no. 10, pp. 1830–1836, 1998, doi: 10.1118/1.598363.

[100] L. Groves, N. Li, T. M. Peters, and E. C. S. Chen, "Towards a first-person perspective mixed reality guidance system for needle interventions," *J. Imag.*, vol. 8, no. 1, Jan. 2022, Art. no. 35212, doi: 10.3390/jimaging8010007.

[101] A. Fedorov et al., "3D slicer as an image computing platform for the quantitative imaging network," *Magn. Reson. Imag.*, vol. 30, no. 9, pp. 1323–1341, Nov. 2012, doi: 10.1016/j.mri.2012.05.001.

[102] P. Schullian, E. W. Johnston, D. Putzer, G. Eberle, G. Laimer, and R. Bale, "Safety and efficacy of stereotactic radiofrequency ablation for very large (≥8 cm) primary and metastatic liver tumors," *Sci. Rep.*, vol. 10, no. 1, Jan. 2020, Art. no. 1618, doi: 10.1038/s41598-020-58383-y.

[103] P. Tinguely et al., "Stereotactic image-guided microwave ablation for malignant liver tumors—A multivariable accuracy and efficacy analysis," *Front. Oncol.*, vol. 10, 2020, Art. no. 25425, doi: 10.3389/fonc.2020.00842.

[104] D. Haemmerich, L. Chachati, A. S. Wright, D. M. Mahvi, F. T. Lee, and J. G. Webster, "Hepatic radiofrequency ablation with internally cooled probes: Effect of coolant temperature on lesion size," *IEEE Trans. Biomed. Eng.*, vol. 50, no. 4, pp. 493–500, Apr. 2003, doi: 10.1109/TBME.2003.809488.

[105] J. Lee, H. Rhim, M. W. Lee, T. W. Kang, K. D. Song, and J. K. Lee, "Direction of tissue contraction after microwave ablation: A comparative experimental study in ex vivo bovine liver," *Korean J. Radiol.*, vol. 23, no. 1, pp. 42–51, Jan. 2022, doi: 10.3348/kjr.2021.0134.

[106] C. Chen et al., "Theoretical evaluation of microwave ablation applied on muscle, fat and bone: A numerical study," *Appl. Sci.*, vol. 11, no. 17, Jan. 2021, Art. no. 8271, doi: 10.3390/app11178271.

[107] D. Haemmerich, A. W. Wright, D. M. Mahvi, F. T. Lee, and J. G. Webster, "Hepatic bipolar radiofrequency ablation creates coagulation zones close to blood vessels: A finite element study," *Med. Biol. Eng. Comput.*, vol. 41, no. 3, pp. 317–323, May 2003, doi: 10.1007/BF02348437.

[108] L. S. Poulou, E. Botsa, I. Thanou, P. D. Ziakas, and L. Thanos, "Percutaneous microwave ablation vs radiofrequency ablation in the treatment of hepatocellular carcinoma," *World J. Hepatol.*, vol. 7, no. 8, pp. 1054–1063, May 2015, doi: 10.4254/wjh.v7.i8.1054.

[109] S. Shetty, R. Kumar, and S. Bharati, "Electrical conductivity spectra of hepatic tumors reflect hepatocellular carcinoma progression in mice," *Biomed. Phys. Eng. Exp.*, vol. 6, no. 6, Oct. 2020, Art. no. 065019, doi: 10.1088/2057-1976/abbbd5.

[110] S. Avadiappan, S. Payabvash, M. A. Morrison, A. Jakary, C. P. Hess, and J. M. Lupo, "A fully automated method for segmenting arteries and quantifying vessel radii on magnetic resonance angiography images of varying projection thickness," *Front. Neurosci.*, vol. 14, Jun. 2020, Art. no. 537, doi: 10.3389/fnins.2020.00537.

[111] D. Martí-Aguado et al., "Automated whole-liver MRI segmentation to assess steatosis and iron quantification in chronic liver disease," *Radiology*, vol. 302, no. 2, pp. 345–354, Feb. 2022, doi: 10.1148/radiol.2021211027.

[112] A. Deshpande et al., "Automatic segmentation, feature extraction and comparison of healthy and stroke cerebral vasculature," *NeuroImage: Clin.*, vol. 30, Jan. 2021, Art. no. 102573, doi: 10.1016/j.nicl.2021.102573.

[113] S. Cai, Z. Wang, S. Wang, P. Perdikaris, and G. E. Karniadakis, "Physics-informed neural networks for heat transfer problems," *J. Heat Transfer*, vol. 143, Apr. 2021, Art. no. 060801, doi: 10.1115/1.4050542.

[114] F. H. Cornelis, C. Marcelin, and J. - C. Bernhard, "Microwave ablation of renal tumors: A narrative review of technical considerations and clinical results," *Diagn. Interventional Imag.*, vol. 98, no. 4, pp. 287–297, Apr. 2017, doi: 10.1016/j.diii.2016.12.002.

[115] D. Putzer, P. Schullian, G. Eberle, and R. J. Bale, "Thermal ablation—An option in curative treatment of HCC," *Memo*, vol. 13, no. 2, pp. 207–211, Jun. 2020, doi: 10.1007/s12254-020-00600-5.

[116] F. Piñero, M. Dirchwolf, and M. G. Pessôa, "Biomarkers in hepatocellular carcinoma: Diagnosis, prognosis and treatment response assessment," *Cells*, vol. 9, no. 6, Jun. 2020, Art. no. 1370, doi: 10.3390/cells9061370.

[117] A. K. Singh, R. Kumar, and A. K. Pandey, "Hepatocellular carcinoma: Causes, mechanism of progression and biomarkers," *Curr. Chem. Genomic. Transl. Med.*, vol. 12, pp. 9–26, Jun. 2018, doi: 10.2174/2213988501812010009.

[118] N. Yoneda et al., "Current status of imaging biomarkers predicting the biological nature of hepatocellular carcinoma," *Japanese J. Radiol.*, vol. 37, no. 3, pp. 191–208, Mar. 2019, doi: 10.1007/s11604-019-00817-3.